

Predicting Frictional Properties of Graphene Kirigami Using Molecular Dynamics and Neural Networks

Designs for a negative friction coefficient.

Mikkel Metzsch Jensen



Thesis submitted for the degree of
Master in Computational Science: Materials Science
60 credits

Department of Physics
Faculty of mathematics and natural sciences

UNIVERSITY OF OSLO

Spring 2023

Predicting Frictional Properties of Graphene Kirigami Using Molecular Dynamics and Neural Networks

Designs for a negative friction coefficient.

Mikkel Metzsch Jensen



© 2023 Mikkel Metzsch Jensen

Predicting Frictional Properties of Graphene Kirigami Using Molecular Dynamics and Neural Networks

<http://www.duo.uio.no/>

Printed: Reprosentralen, University of Oslo

Abstract

Basic introduction

Various numerical models and experimental results propose different governing mechanisms for friction at the nanoscale.

More detailed background

We consider a graphene sheet modified with Kirigami-inspired cuts and under the influence of strain. Prior research has demonstrated that this system exhibits out-of-plane buckling, which could result in a decrease in contact area when sliding on a substrate. According to asperity theory, this decrease in contact area is expected to lead to a reduction in friction.

General problem

However, to the best of our knowledge, no previous studies have investigated the friction behavior of a nanoscale Kirigami graphene sheet under strain.

Summarize main result: “here we show”

Here we show that specific Kirigami designs yield a non-linear dependency between kinetic friction and the strain of the sheet.

General context

Using molecular dynamics simulation, we have found a non-monotonic increase in friction with strain. We found that the friction-strain relationship does not show any clear dependency on contact area which contradicts asperity theory. Our findings suggest that the effect is associated with the out-of-plane buckling of the graphene sheet and we attribute this to a commensurability effect. By mimicking a load-strain coupling through tension, we were able to utilize this effect to demonstrate a negative friction coefficient on the order of -0.3 for loads in the range of a few nN. In addition, we have attempted to use machine learning to capture the relationship between Kirigami designs, load, and strain, with the objective of performing an accelerated search for new designs. While this approach produced some promising results, we conclude that further improvements to the dataset are necessary in order to develop a reliable model.

Broader perspective

We anticipate our findings to be a starting point for further investigations of the underlying mechanism for the frictional behavior of a Kirigami sheet. For instance, the commensurability hypothesis could be examined by varying the sliding angle in simulations. We propose to use an active learning strategy to extend the dataset for the use of machine learning to assist these investigations. If successful, further studies can be done on the method of inverse design. In summary, our findings suggest that the application of nanoscale Kirigami can be promising for developing novel friction-control strategies.

353 words

Various numerical models and experimental results propose different governing mechanisms for friction at the nanoscale. We consider a graphene sheet modified with Kirigami-inspired cuts and under the influence of strain. Prior research has demonstrated that this system exhibits out-of-plane buckling, which could result in a decrease in contact area when sliding on a substrate. According to asperity theory, this decrease in contact area is expected to lead to a reduction in friction. However, to the best of our knowledge, no previous studies have investigated the friction behavior of a nanoscale Kirigami graphene sheet under strain. Here we show that specific Kirigami designs yield a non-linear dependency between kinetic friction and the strain of the sheet. Using molecular dynamics simulation, we have found a non-monotonic increase in friction with strain. We found that the friction-strain relationship does not show any clear dependency on contact area which contradicts asperity theory. Our findings suggest that the effect is associated with the out-of-plane buckling of the graphene sheet and we attribute this to a commensurability effect. By mimicking a load-strain coupling through tension, we were able to utilize this effect to demonstrate a negative friction coefficient on the order of -0.3 for loads in the range of a few nN. In addition, we have attempted to use machine learning to capture the relationship between Kirigami designs, load, and strain, with the objective of performing an accelerated search for new designs. While this approach produced some promising results, we conclude that further improvements to the dataset are necessary in order to develop a reliable model. We anticipate our findings to be a starting point for further investigations of the underlying mechanism for the frictional behavior of a Kirigami sheet. For instance, the commensurability hypothesis could be examined by varying the sliding angle in simulations. We propose to use an active learning strategy to extend the dataset for the use of machine learning to assist these investigations. If successful, further studies can be done on the method of inverse design. In summary, our findings suggest that the application of nanoscale Kirigami can be promising for developing novel friction-control strategies.

Acknowledgments

Acknowledgments.

List of Symbols

F_N Normal force (normal load)

Acronyms

CM Center of Mass. 13, 14

GAN Generative Adversarial Networks. 2, 33

LJ Lennard-Jones. 17, 18

MD Molecular Dynamics. 1, 2, 3, 4, 9, 10, 20, 22, 29, 30, 31

ML Machine Learning. 2, 10, 32

std Standard Deviation. 15, 16, 19, 20

Contents

1	Introduction	1
1.1	Motivation	1
1.2	Goals	3
1.3	Contributions	3
1.4	Thesis structure	4
I	Background Theory	5
II	Simulations	7
2	Pilot study	9
2.1	Friction simulation parameters	9
2.2	Force traces	9
2.2.1	Force oscillations	9
2.2.2	Decompositions	13
2.2.3	Center of mass path	13
2.3	Defining metrics for friction	15
2.3.1	Kinetic friction	15
2.3.2	Static friction	16
2.4	Out-of-plane buckling	16
2.5	Investigating default parameters	19
2.5.1	Computational cost	20
2.6	Load and stretch dependencies	22
2.6.1	Pressure reference for normal load	22
2.6.2	Strain dependency	22
2.6.3	Load dependency	24
2.6.4	Prospects of a negative friction coefficient	27
3	Summary	29
3.1	Summary and conclusions	29
3.1.1	Designing an MD simulation	29
3.1.2	Generetig Kirigami patterns	30
3.1.3	Control friction using Kirigami	30
3.1.4	Capturing trends in friction data with machine learning	31
3.1.5	Accelerated search	32
3.1.6	Negative friction coefficient	32
3.2	Outlook	33
	Appendices	35
A	Appendix A	37

A	Appendix B	39
B	Appendix C	41

Chapter 1

Introduction

1.1 Motivation

Friction is the force that prevents the relative motion of objects in contact. From our everyday life, we recognize it as the inherent resistance to sliding motion. Some surfaces appear slippery and some rough, and we know intuitively that sliding down a snow-covered hill is much more exciting than its grassy counterpart. Without friction, it would not be possible to walk across a flat surface, lean against the wall without falling over or secure an object by the use of nails or screws [p. 5] [1]. It is probably safe to say that the concept of friction is integrated into our everyday life to such an extent that most people take it for granted. However, the efforts to control friction date back to the early civilization (3500 B.C.) with the use of the wheel and lubricants to reduce friction in translational motion [2]. Today, friction is considered a part of the wider field *tribology* derived from the Greek word *tribos* meaning “rubbing” and includes the science of friction, wear and lubrication [2]. The most compelling motivation to study tribology is ultimately to gain full control of friction and wear for various technical applications. Especially, reducing friction is of great interest as this has advantages for energy efficiency. It has been reported that tribological problems have a significant potential for economic and environmental improvements [3]:

“On global scale, these savings would amount to 1.4% of the GDP annually and 8.7% of the total energy consumption in the long term.” [4].

On the other hand, the reduction of friction is not the only sensible application for tribological studies. Controlling frictional properties, besides minimization, might be of interest in the development of a grasping robot where finetuned object handling is required. While achieving a certain “constant” friction response is readily obtained through appropriate material choices, we are yet to unlock the full capabilities to alter friction dynamically on the go. One example from nature inspiring us to think along these lines are the gecko feet. More precisely, the Tokay gecko has received a lot of attention in scientific studies aiming to unravel the underlying mechanism of its “toggleable” adhesion properties. Although geckos can produce large adhesive forces, they retain the ability to remove their feet from an attachment surface at will [5]. This makes the gecko able to achieve a high adhesion on the feet when climbing a vertical surface while lifting them for the next step remains relatively effortless. For a grasping robot, we might consider an analog frictional concept of a surface material that can change from slippery to rough on demand depending on specific tasks; Slippery and smooth when interacting with people and rough and firmly gripping when moving heavy objects.

In recent years an increasing amount of interest has gone into the studies of the microscopic origin of friction, due to the increased possibilities in surface preparation and the development of nanoscale experimental methods. Nano-friction is also of great concern for the field of nano-machining where the frictional properties between the tool and the workpiece dictate machining characteristics [3]. With concurrent progress in computational capacity and development of Molecular Dynamics (MD), numerical investigations serve as an invaluable tool for getting insight into the nanoscale mechanics associated with friction. This simulation-based approach can be considered as a “numerical experiment” enabling us to create and probe a variety of high-complexity systems which are still out of reach for modern experimental methods.

In materials science such MD-based numerical studies have been used to explore the concept of so-called *metamaterials* where the material compositions are designed meticulously to enhance certain physical properties [6–11]. This is often achieved either by intertwining different material types or removing certain regions completely. In recent papers by Hanakata et al. [6, 7], numerical studies have showcased that the mechanical properties of a graphene sheet, yield stress and yield strain, can be altered through the introduction of so-called *Kirigami* inspired cuts into the sheet. Kirigami is a variation of origami where the paper is cut additionally to being folded. While these methods originate as an art form, aiming to produce various artistic objects, they have proven to be applicable in a wide range of fields such as optics, physics, biology, chemistry and engineering [12]. Various forms of stimuli enable direct 2D to 3D transformations through folding, bending, and twisting of microstructures. While original human designs have contributed to specific scientific applications in the past, the future of this field is highly driven by the question of how to generate new designs optimized for certain physical properties. However, the complexity of such systems and the associated design space makes for seemingly intractable¹ problems ruling out analytic solutions.

Earlier architecture design approaches such as bioinspiration, looking at gecko feet for instance, and Edisonian, based on trial and error, generally rely on prior knowledge and an experienced designer [9]. While the Edisonian approach is certainly more feasible through numerical studies than real-world experiments, the number of combinations in the design space rather quickly becomes too large for a systematic search, even when considering the computation time on modern-day hardware. However, this computational time constraint can be relaxed by the use of machine learning (ML) which has proven successful in the establishment of a mapping from the design space to physical properties of interest. This gives rise to two new styles of design approaches: One, by utilizing the prediction from a trained network we can skip the MD simulations altogether resulting in an *accelerated search* of designs. This can be further improved by guiding the search accordingly to the most promising candidates, for instance, as done with the *genetic algorithm* based on mutation and crossing of the best candidates so far. Another more sophisticated approach is through generative methods such as *Generative Adversarial Networks* (GAN) or diffusion models. The latter is being used in state-of-the-art AI systems such as OpenAI’s DALL-E2 [13] or Midjourney [14]. By working with a so-called *encoder-decoder* network structure, one can build a model that reverses the prediction process. This is often referred to as *reverse design*, where the model predicts a design from a set of physical target properties. In the papers by Hanakata et al. [6, 7] both the *accelerated search* and the *inverse design* approach was proven successful to create novel metamaterial Kirigami designs with the graphene sheet.

Hanakata et al. attributes the variation in mechanical properties to the non-linear effects arising from the out-of-plane buckling of the sheet. Since it is generally accepted that the surface roughness is of great importance for frictional properties it can be hypothesized that Kirigami-induced out-of-plane buckling can also be exploited for the design of frictional metamaterials. For certain designs, we might hope to find a relationship between the stretching of the sheet and frictional properties. If significant, this could give rise to an adjustable friction behavior beyond the point of manufacturing. For instance, the grasping robot might apply such a material as artificial skin for which stretching or relaxing of the surface could result in a changeable friction strength.

In addition, the Kirigami graphene properties can be explored through a potential coupling between the stretch and the normal load, through a nanomachine design, with the aim of altering the friction coefficient. This invites the idea of non-linear friction coefficients which might in theory also take on negative values. The latter would constitute a rare property only found a few cases. These are mainly for the unloading phase of adhesive surfaces [15] or the loading phase of particular heterojunction materials [16, 17].

To the best of our knowledge, Kirigami has not yet been implemented to alter the frictional properties of a nanoscale system. However, in a recent paper by Liefferink et al. [18] it is reported that macroscale Kirigami can be used to dynamically control the macroscale roughness of a surface through stretching. They reported that the roughness change led to a changeable frictional coefficient by more than one order of magnitude. This supports the idea that Kirigami designs can be used to alter friction, but we believe that taking this concept to the nanoscale would involve a different set of governing mechanisms and thus contribute to new insight in this field.

¹In computer science we define an *intractable* problem as a problem with no *efficient* algorithm to solve it nor any analytical solutions. The only way to solve such problems is the *brute-force* approach, simply trying all possible solutions, which is often beyond the capabilities of computational resources.

1.2 Goals

In this thesis, we investigate the prospects of altering the frictional properties of a graphene sheet through the application of Kirigami-inspired cuts and stretching of the sheet. With the use of molecular dynamics (MD) simulations, we evaluate the frictional properties of various Kirigami designs under different physical conditions. Based on the MD results, we investigate the possibility to use machine learning for the prediction of frictional properties and subsequently using the model for an accelerated search of new designs. The main goals of the thesis can be summarized as follows.

1. Design an MD simulation procedure to evaluate the frictional properties of a Kirigami graphene sheet under specified physical conditions.
2. Develop a numerical framework to generate various Kirigami designs, both by seeking inspiration from macroscale designs and by the use of a random walk based algorithm.
3. Investigate the frictional behavior under varying load and stretch for different Kirigami designs.
4. Develop and train a machine learning model to predict the MD simulation result and perform an accelerated search of new designs with the scope of optimizing certain frictional properties.

1.3 Contributions

By working towards the goals outlined above (Sec. 1.2), I have discovered a non-linear relationship between the kinetic friction and the strain for certain Kirigami patterns. This phenomenon was found to be associated with the out-of-plane buckling of the Kirigami sheet but with no clear relationship to the contact area or the tension in the sheet. I found that this method does not provide any mechanism for a reduction in friction, in comparison to a non-cut sheet, but the straining of certain Kirigami sheets allows for a non-monotonic increase in friction. The relationship to normal load was proven negligible in this context and I have demonstrated that a coupled system of load and strain (through sheet tension) can exhibit a negative friction coefficient in certain load ranges. Moreover, I have created a dataset of roughly 10,000 data points for assessing the employment of machine learning and accelerated search of Kirigami designs. I have found, that this approach might be useful, but it requires an extended dataset in order to produce reliable results for a search of new designs.

During our investigations, I have built three numerical tools, beyond the regular scripts associated with data analysis, which can be found on Github [19]. The tools are summarized in the following.

- I have written a LAMMPS-based [20] tool for simulating and measuring the frictional properties of a graphene sheet sliding on a substrate. The code is generally made flexible concerning the choice of sheet configuration, system size, simulation parameters and MD potentials, which makes it applicable for further studies within this topic. I have also built an automated procedure to carry out multiple simulations under varying parameters by submitting jobs to a computational cluster via an ssh connection. This was done by adding minor additions to the python package developed by E. M. Nordhagen [21].
- I have generated a Python-based tool for generating Kirigami patterns and exporting these in a compatible format with the simulation software. The generation of molecular structures is done with the use of ASE [22]. Our software includes two classes of patterns inspired by macroscale designs and a random walk algorithm which allow for a variety of different designs through user-defined biases and constraints. Given our system size of choice, the first two pattern generators are capable of generating on the order of 10^8 unique designs while the random walk generator allows for significantly more.
- I have built a machine learning tool based on Pytorch [23] which includes setting up the data loaders, a convolutional network architecture, a loss function, and general algorithms for training and validating the results. Additionally, I have written several scripts for performing grid searches and analyzing the model predictions in the context of the frictional properties of graphene.

All numerical implementations used for this thesis have been originally developed for the purpose with the exception of the usage of libraries as mentioned above and commonly known Python libraries such as Numpy and Matplotlib.

1.4 Thesis structure

The thesis is divided into two parts. In Part **I** we introduce the relevant theoretical background, and in Part **II** we present the numerical implementations and the results of this thesis.

Part **I** contains a description of the theoretical background related to Friction (??), Molecular Dynamics (??) and Machine Learning (??). In ?? we formulate our research questions in the light of the friction theory.

In Part **II**, we begin by presenting our definition and setting up of the system in ???. This includes the MD simulations and the generation of Kirigami designs. This is followed by a pilot study in Chapter 2 where we evaluate the simulation results for various physical conditions and compare a non-cut sheet to two different Kirigami designs. Further explorations of the Kirigami configurations are carried out in ??? which includes the generation of a dataset and the employment of machine learning and an accelerated search. We use the results from the pilot study to demonstrate the possibility to achieve a negative friction coefficient for a system with coupled load and strain in ???. Finally, we summarize our results and provide an outlook for further studies in Chapter 3. Additional figures are shown in ??, ?? and ??.

Part I

Background Theory

Part II

Simulations

Chapter 2

Pilot study

In this chapter, we begin by analyzing the frictional properties of our system. Initially, we examine the results for a non-cut sheet to establish suitable metrics for a numerical evaluation of friction and validate our parameter choices. This provides a basis for the following study where we explore the frictional properties of the Tetrahedron and Honeycomb Kirigami patterns. We conduct a more thorough investigation of the friction dependencies to temperature, sliding speed, spring constant, and timestep. Finally, we investigate the average friction across all three configurations when subjected to strain, including an examination of the relationship to contact area and the friction-load curves.

2.1 Friction simulation parameters

The MD simulations we will carry out to measure friction are governed by a small set of parameters. Since we aim to develop a machine learning model, it is necessary to standardize these parameters. Therefore, we keep the majority of the parameters constant and only modify a small subset of them, which includes sheet configuration, strain, and load. Instead of starting with the parameter selection process, we first state the final choice in Table 2.1. Due to the great number of parameters, we did not make an exhaustive search of all parameters before deciding on the final choice. Instead, we have taken a basis in parameters used in similar friction simulations [24–28] and adjusted accordingly to the aim of getting stable measurements and reducing computation time where possible. Parameters such as initial relaxation time, pauses and strain speed are chosen mainly from the results of initial stability tests. That is, we visually verify that the system is close to an equilibrium state and that it does not carry momentum before going to the next step in the numerical procedure. The sheet and pull block sizes are chosen with a consideration of the balance between Kirigami design options and computational resources. The scan direction is selected to be parallel with the connecting line between the pull blocks. This choice is made primarily to minimize the complexity of the motion, as it is hypothesized that other scan directions might cause the center of the sheet to lag behind and produce a slight side flexion. The remaining parameters: Temperature T , sliding speed v_{slide} , spring constant K , normal load F_N , timestep dt and sliding distance have been chosen because the friction output remains relatively stable with moderate perturbations around these default values. We will explain this in more detail later in the chapter. Note that the default values in Table 2.1 will be used when nothing else is stated explicitly.

2.2 Force traces

We begin by assessing the friction force traces, i.e. force vs. time curves, for a single friction simulation using the default parameters shown in Table 2.1 for a non-cut sheet with no stretch applied and a normal load of 1 nN.

2.2.1 Force oscillations

We evaluate the friction force as the force acting on the sheet from the substrate. We consider initially the force component F_{\parallel} parallel to the sliding direction shown in Fig. 2.1. We use a sample rate of $10 \text{ ps}^{-1} = 100 \text{ timesteps}^{-1}$ for which each sample is the mean value of the preceding 100 timesteps. We observe immediately that the data

Table 2.1: Parameters involved in the numerical MD simulation for measuring friction. The default values correspond to the final choice used for the dataset. The shaded cells denote the parameters varied in the ML dataset.

Parameter	Default value	Description
T	300 K	Temperature of the system.
v_{slide}	20 m/s	Sliding speed for the sheet.
K	∞	Spring constant for the coupling between the virtual atom and the sheet pull blocks.
Scan direction	$(x, y) = (0, 1)$ (zigzag direction)	The direction of sliding.
Sheet configuration	Contiguous	Binary mapping describing which atoms are removed (0) and which are still present (1) in the graphene sheet.
Strain amount	[0, rupture]	The ratio of change in length to the original length.
F_N	[0.1, 10] nN	Applied normal force to the pull blocks.
dt	1 fs	MD integration timestep.
Initial relaxation time	15 ps	Initial relaxation time before straining.
Pauses	5 ps	Relaxation pauses after strain, and during the normal load phase (before sliding).
Strain Speed	0.01 ps^{-1}	The rate of straining for the sheet.
Slide distance	400 Å	How far the sheet is slid.
Sheet size	$130.029 \times 163.219 \text{ Å}$	Spatial 2D size of the sheet.
Pull block size	$2 \times 130.029 \times 15.183 \text{ Å}$	Spatial 2D size of the pull blocks.

carries oscillations on different time scales which match our general expectations for sliding involving periodic surfaces. By applying a Savgol filter to the data with a polynomial order of 5 and a window length of 150 timesteps (corresponding to a sliding distance of 3 Å or a time window of 15 ps) we can qualitatively point out at least two different frequencies of oscillation. During the first 10 Å of sliding, seen in Fig. 2.1a, we see roughly three waves on the Savgol filter corresponding to a relatively high frequency, while for the duration of 100 Å of sliding, seen in Fig. 2.1b, the same Savgol filter reveals a lower frequency on top, creating the visual pattern of a wavepacket. The data does not indicate signs of stick-slip behavior as otherwise found in other studies, e.g. by Zhu and Li [27] for graphene on gold, who saw a more typical saw tooth shape in the force trace. Besides the difference in the substrate material, using gold instead of silicon, they used a lower sliding speed of 10 m/s and a soft spring of $K = 10 \text{ N/m}$. By adopting these parameters we get a slightly different force trace behavior as shown in Fig. 2.1c and Fig. 2.1d. This parameter change results in a loss of symmetry in the force oscillations, but it still does not produce any significant discontinuities in the trace. By keeping the spring constant $K = 10 \text{ N/m}$ and lowering the sliding speed further down to 1 m/s we achieve a proper stick-slip behavior as shown in Fig. 2.1e and Fig. 2.1f. Considering all three simulations, we might classify the results from the default settings, $K = \infty, v = 20 \text{ m/s}$, as smooth sliding, $K = 10 \text{ N/m}, v = 10 \text{ m/s}$, as a transition phase with possible occasional slipping, and $K = 10 \text{ N/m}, v = 1 \text{ m/s}$ as a typical stick-slip behaviour. This confirms the qualitative observation that stick-slip behavior is suppressed with stiff springs [29] springs and high sliding velocity [26]. Having a low sliding speed comes with a high computational cost which is the reason that we choose a relatively high sliding speed of 20 m/s. The choice of an infinite spring constant is related to the stability of the measurements and is discussed later in this chapter.

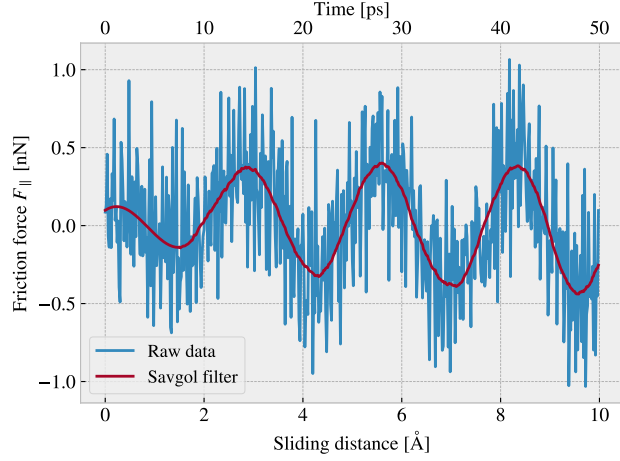
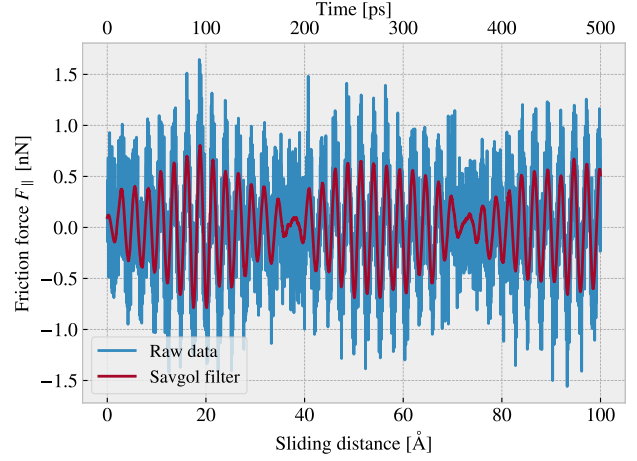
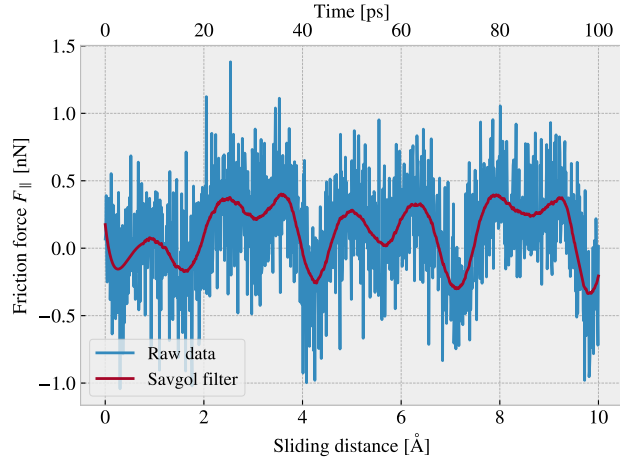
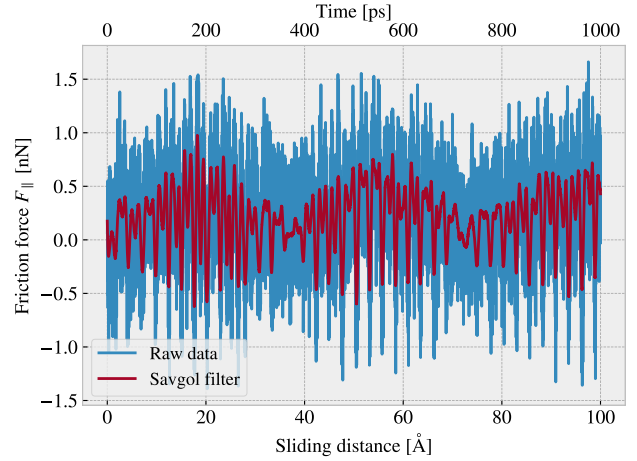
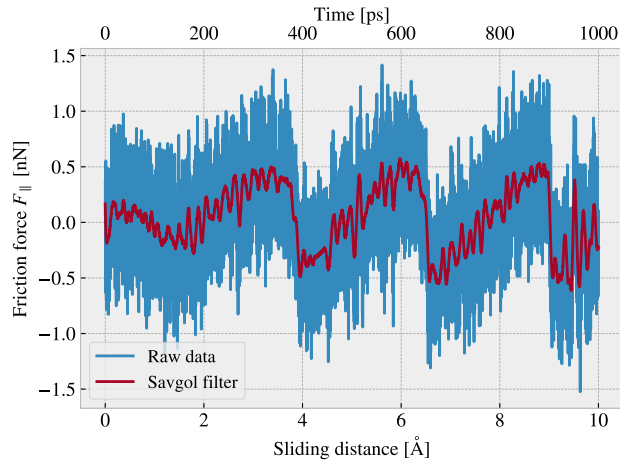
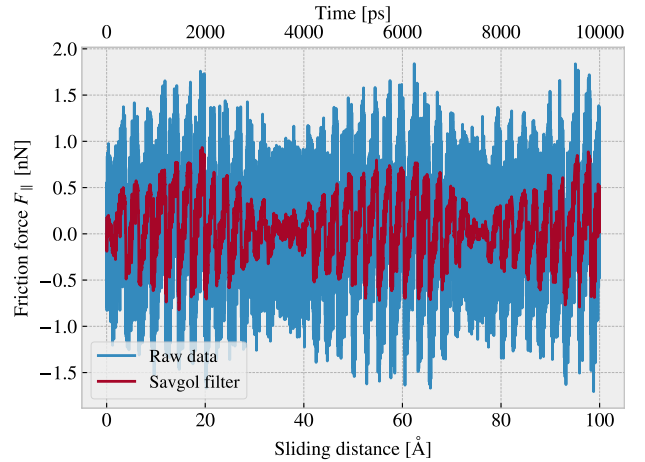
(a) $K = \text{inf}$, $v = 20 \frac{\text{m}}{\text{s}}$ (10 Å sliding).(b) $K = \text{inf}$, $v = 20 \frac{\text{m}}{\text{s}}$ (100 Å sliding).(c) $K = 10 \frac{\text{N}}{\text{m}}$, $v = 10 \frac{\text{m}}{\text{s}}$ (10 Å sliding).(d) $K = 10 \frac{\text{N}}{\text{m}}$, $v = 10 \frac{\text{m}}{\text{s}}$ (100 Å sliding).(e) $K = 10 \frac{\text{N}}{\text{m}}$, $v = 1 \frac{\text{m}}{\text{s}}$ (10 Å sliding).(f) $K = 10 \frac{\text{N}}{\text{m}}$, $v = 1 \frac{\text{m}}{\text{s}}$ (100 Å sliding).

Figure 2.1: Force traces of the friction force component F_{\parallel} parallel to the sliding direction acting from the substrate on the full sheet. The force traces are plotted against the sliding distance (lower x-axis) and the corresponding sliding time (upper x-axis). The sliding distance is measured by the displacement of the virtual atom tethering the sheet. The red line represents a Savgol filter with polynomial order 5 and a window length of 150 timesteps (corresponding to a sliding distance of 3 Å or a time window of 15 ps). Each row, (a,b), (c,d), (e,f), represents a different choice of the spring constant K and sliding speed v , while the columns show the same result for two different time scales. The default settings are represented in figure (a) and (b).

By performing a Fourier Transform on the data, using the default parameters, we can quantify the leading frequencies observed in Fig. 2.1a and Fig. 2.1b. The Fourier transform is shown in Fig. 2.2a, and by plotting the two most dominant frequencies $f_1 = 0.0074 \text{ ps}^{-1}$ and $f_2 = 0.0079 \text{ ps}^{-1}$ as a sine sum, $\sin(2\pi f_1) + \sin(2\pi f_2)$, we find a qualitatively convincing fit to the observed wavepacket shape as seen in Fig. 2.2b. We can convert the frequencies according to that of a wavepacket. By using the trigonometric identity

$$\begin{aligned}\sin(a+b) &= \sin(a)\cos(b) + \cos(a)\sin(b), \\ \sin(a-b) &= \sin(a)\cos(b) - \cos(a)\sin(b),\end{aligned}$$

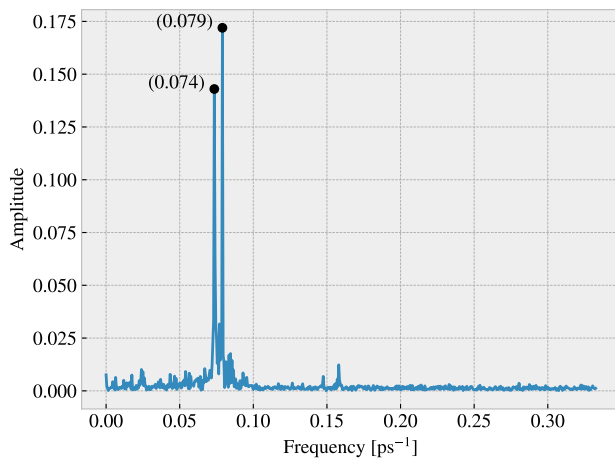
and decomposing the frequencies as $f_1 = a - b$, $f_2 = a + b$, we can rewrite the sine sum as the sinusoidal product

$$\begin{aligned}\sin(2\pi f_1) + \sin(2\pi f_2) &= \sin(2\pi(a-b)) + \sin(2\pi(a+b)) \\ &= \sin(2\pi a)\cos(2\pi b) + \cos(2\pi a)\sin(2\pi b) + \sin(2\pi a)\cos(2\pi b) - \cos(2\pi a)\sin(2\pi b) \\ &= 2\sin(2\pi a)\cos(2\pi b),\end{aligned}$$

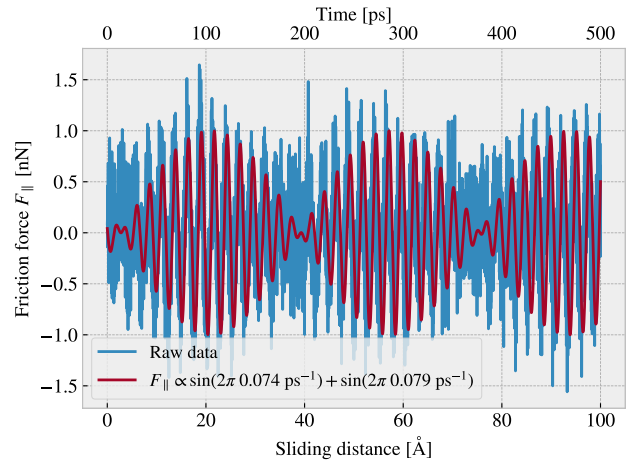
with

$$\begin{aligned}a = \frac{f_1 + f_2}{2} &= 0.0763 \pm 0.0005 \text{ ps}^{-1}, & b = \frac{f_2 - f_1}{2} &= 0.0028 \pm 0.0005 \text{ ps}^{-1}, \\ &= 0.381 \pm 0.003 \text{ \AA}^{-1}, & &= 0.014 \pm 0.003 \text{ \AA}^{-1}.\end{aligned}$$

In the latter transition, we have denoted the frequency with respect to the sliding distance by considering the default sliding speed of $20 \text{ m/s} = 0.2 \text{ \AA/ps}$. This makes us recognize the high oscillation frequency as a and the low frequency as b . The faster one has a period of $T_a = 2.62 \pm 0.02 \text{ \AA}^2$ which corresponds well with the magnitude of the lattice spacing as expected theoretically, and especially that of graphene with a lattice constant of 2.46 \AA . The longer period $T_b = 71 \pm 15 \text{ \AA}$ is not obviously explained. We notice a similarly long period oscillation for all three cases Fig. 2.1b, Fig. 2.1d and Fig. 2.1f, and thus we have no reason to believe that this is dependent on the stick-slip behavior. The initial build-up in friction force is reminiscent of friction strengthening, which is often reported [24, 30], but the periodicity goes against this idea. Instead, we might attribute it to a phonon resonance effect which might be further affected by the fact that we use periodic boundary conditions for a finite substrate.



(a) FT result shown for a reduced frequency range.



(b) Two most dominant frequencies applied to the data from Fig. 2.1b

Figure 2.2: Fourier transform analysis of the force traces shown in Fig. 2.1a and Fig. 2.1b, but with the use of all 400 \AA of sliding. (a) The two most dominant frequency peaks from the Fourier analysis. Note that we cut off higher frequencies from the plot since no significant peaks were found there. (b) A comparison between the raw data and the wavefunction corresponding to the two peaks in panel (a).

²The uncertainty Δy is calculated as $\Delta y = \left| \frac{\partial y}{\partial x} \Delta x \right|$ for uncertainty Δx and $y(x)$.

2.2.2 Decompositions

In the previous analysis, we considered the friction force acting on the entire sheet, including the rigid pull blocks, and with respect to the sliding direction. We found this way of measuring the friction force to be the most intuitive and reliable, but we will present the underlying arguments for this choice in the following.

Since we are only applying cuts to the inner sheet, and not the pull blocks, it might appear more natural to only consider friction on the inner sheet. If the desired frictional properties can be achieved by altering the inner sheet one can argue that any opposing effects from the pull blocks can be mitigated by simply adjusting the size ratio between the inner sheet and the pull blocks. However, when looking at the force traces decomposed with respect to the inner sheet and pull block regions respectively in Fig. 2.3a, we observe that the friction force arising from those parts is seemingly antisymmetric. That is, the frictional force exerted by the substrate on the sheet oscillates between the inner sheet and the pull blocks. Keeping in mind that normal force is only applied to the pull blocks we might take this as an intrinsic feature of the system that does not necessarily disappear with a scaling of the size ratio. Any interesting friction properties might depend on this internal distribution of forces. Hence, we hedge our bets and use the full sheet friction force as a holistic approach to avoid excluding relevant features in the measurement data.

Similarly, we might question the decision of only considering the frictional force projected onto the sliding direction as we are then neglecting the “side shift” induced during sliding. In Fig. 2.3b we show the decomposition in terms of the force components parallel F_{\parallel} and perpendicular F_{\perp} to the sliding direction respectively. We notice that the most dominant trend appears for the parallel component. One way to include the perpendicular component is to evaluate friction as the length of the force vector instead. However, this would remove the sign of the force direction and shift the mean friction force up as we see both negative and positive contributions in the parallel force trace. One option to accommodate this issue is by using the vector length for the magnitude but keeping the sign from the parallel component. However, we omit such compromises as this might make the measurement interpretation unnecessarily complex, and we use only the parallel component going forward.

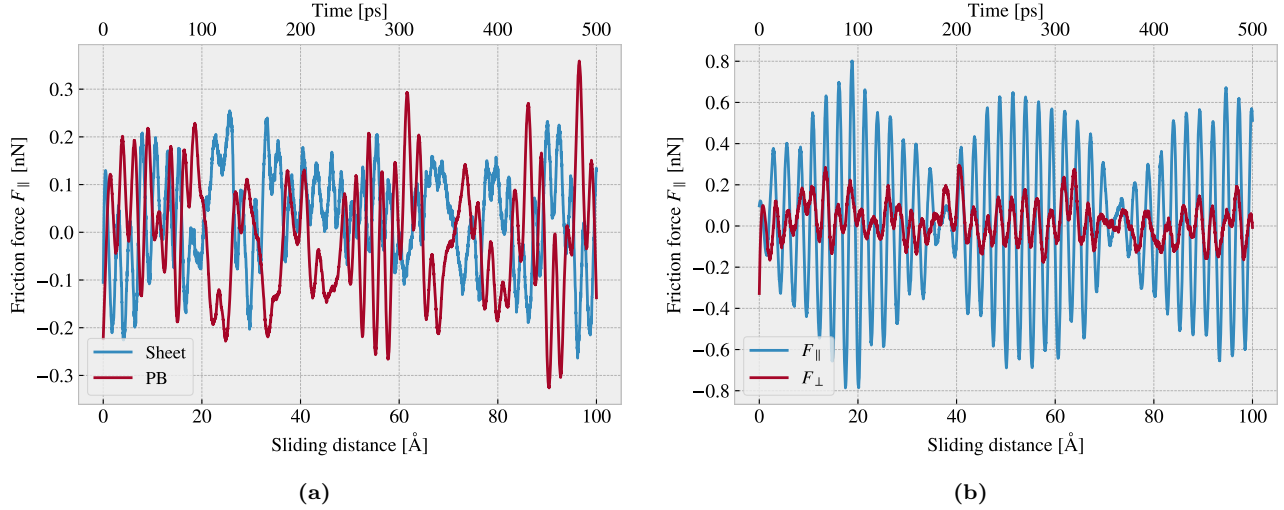


Figure 2.3: Friction force decomposition on the default parameter force trace shown in Fig. 2.1. We show only the Savgol filters here. (a) Decomposition into the sheet regions inner sheet (sheet) and pull blocks (PB). (b) Decomposition into friction force parallel (F_{\parallel}) and perpendicular (F_{\perp}) to the sliding direction.

2.2.3 Center of mass path

From the previous observations of the force traces in Fig. 2.1 we found both smooth sliding and stick-slip behavior depending on the sliding speed and spring constant. Considering the force decomposition in Fig. 2.3b we know that a frictional force in the perpendicular direction to sliding is also present. By looking at the x, y -position for the sheet Center of Mass (CM) we find a qualitatively different behavior when reconsidering the spring constants and sliding speeds investigated in Fig. 2.1. These results are shown in Fig. 2.4. The default case in Fig. 2.4a shows a rather straight path with only a small side motion in comparison to the cases in Fig. 2.4b and Fig. 2.4c.

However, the CM accelerates and deaccelerates with a high frequency, much too high to be associated with the lattice spacing on the order of 2.46 \AA . One possible explanation is that the sheet and substrate constitute an incommensurate contact for which traveling kink excitations make the atoms move in such a way that the sheet CM is incremented in small “bursts”. When looking at the $K = 10 \frac{\text{N}}{\text{m}}$, $v = 10 \frac{\text{m}}{\text{s}}$ case in Fig. 2.4b we see a completely different CM path where the rapid movements align visually better with the force oscillations shown earlier in Fig. 2.1d. The CM accelerates forward and then deaccelerates in combination with a side motion that leads to the CM path making a loop as it slows down. Finally we have the $K = 10 \frac{\text{N}}{\text{m}}$, $v = 10 \frac{\text{m}}{\text{s}}$ in Fig. 2.4b which is confirmed to have stick-slip behavior in Fig. 2.1f. Here the CM path shows a more chaotic movement between accelerations, but with the rapid parts aligning visually well with the timing of the slips seen in Fig. 2.1f. We might associate the chaotic motion with thermal contributions as these are thought to be dominant at lower sliding speeds.

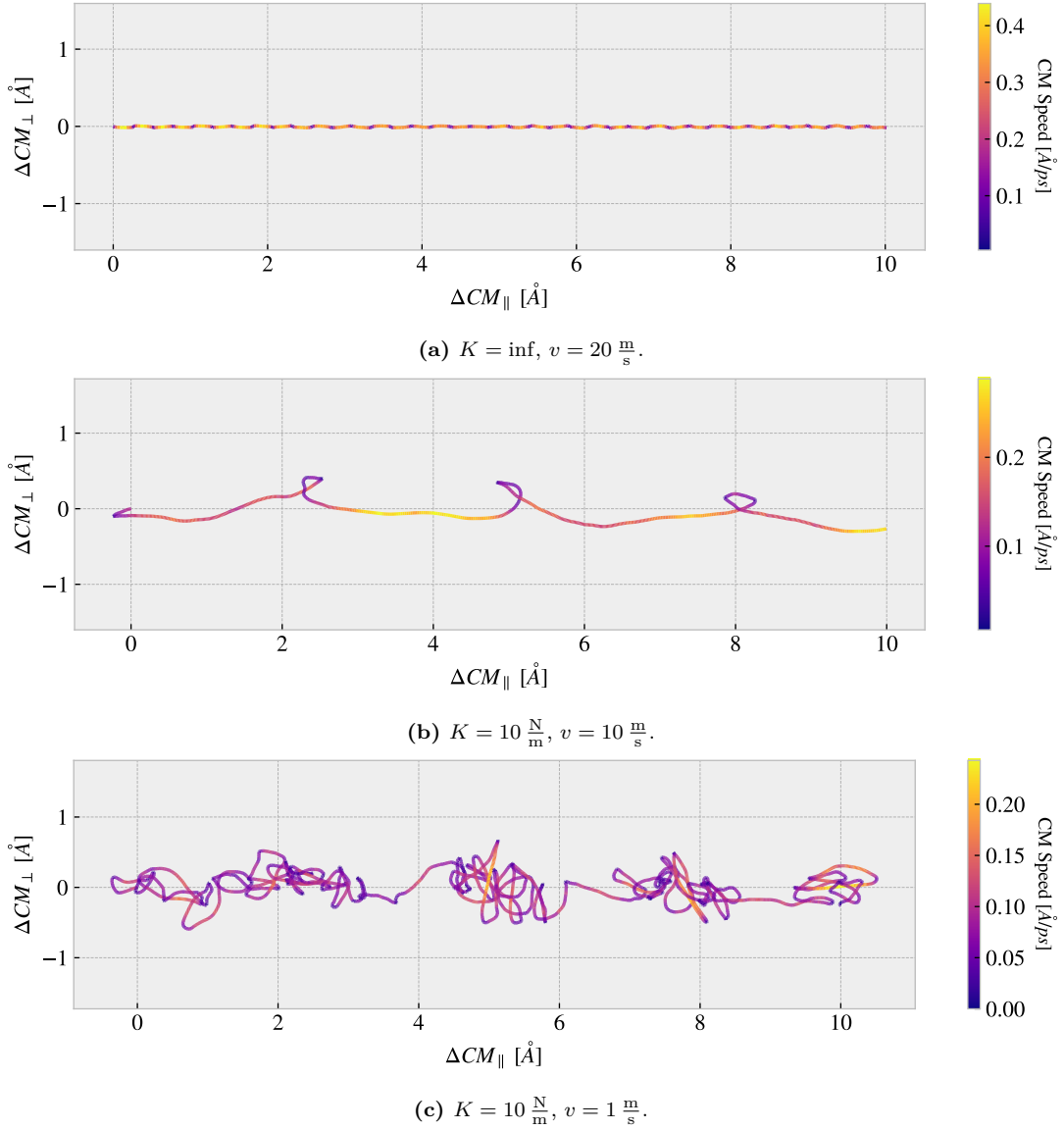


Figure 2.4: Sheet Center of Mass (CM) position relative to the start of the sliding phase in terms of the direction parallel to the sliding direction ΔCOM_{\parallel} and the axis perpendicular to the sliding direction ΔCOM_{\perp} . The colors denote the absolute speed of the CM motion. Figure (a)-(c) shows different parameters used for the spring constant K and sliding speed v similar to that used in Fig. 2.1. (a) Default: $K = \text{inf}$, $v = 20 \frac{\text{m}}{\text{s}}$. (b) Values adopted from Zhu and Li [27]: $K = 10 \frac{\text{N}}{\text{m}}$, $v = 10 \frac{\text{m}}{\text{s}}$. (c) $K = 10 \frac{\text{N}}{\text{m}}$, $v = 1 \frac{\text{m}}{\text{s}}$.

2.3 Defining metrics for friction

In order to evaluate the frictional properties of the sheet we aim to reduce the force trace results, addressed in Sec. 2.2, into single metrics describing the kinetic and static friction respectively.

2.3.1 Kinetic friction

We measure kinetic friction as the mean of the friction force trace. More precisely, we take the mean value of the last half of the dataset in order to ensure that we are sampling from a stable system. For a full sliding simulation of 400 Å our mean value will be founded on the last 200 Å (1000 ps) of sliding. In Fig. 2.5a we have shown the force trace for the first 10 Å of sliding together with a 50% running mean window. The choice of such a short sliding distance is merely to illustrate the sampling procedure, and we see that the final mean estimate (marked with a dot) takes a negative value due to the specific cut-off of the few oscillations captured here. Nonetheless, one approach to quantifying the uncertainty of the final mean estimate is to consider the variation of the running mean preceding the final mean value. The more the running mean fluctuates the more uncertainty associated with the final estimate. Only the running mean “close” to the ending should be considered, since the first part will rely on data from the beginning of the simulation. From the Fourier analysis in Sec. 2.2.1 we found the longest significant oscillation period to be ~ 71 Å. Hence, we find it reasonable to use the standard deviation (std) for the last ~ 71 Å of the running mean window to evaluate the fluctuations. When including the full sliding length this corresponds to the last $\sim 35\%$ of the running mean window ($400 \text{ Å} \cdot 50\% \cdot 35\% \approx 71 \text{ Å}$). We consider the std as an estimate of the absolute error and calculate the relative error by a division of the final mean value. In Fig. 2.5b we showcase a running relative error based on the std, with a window of length 35% the mean window, in a continuation of the illustrative case of a 10 Å sliding from Fig. 2.5a. In this case, we get an extremely high relative error of $\sim 257\%$, but this is consistent with the fact that the short sampling period leads to an unphysical negative value which should be associated with high uncertainty.

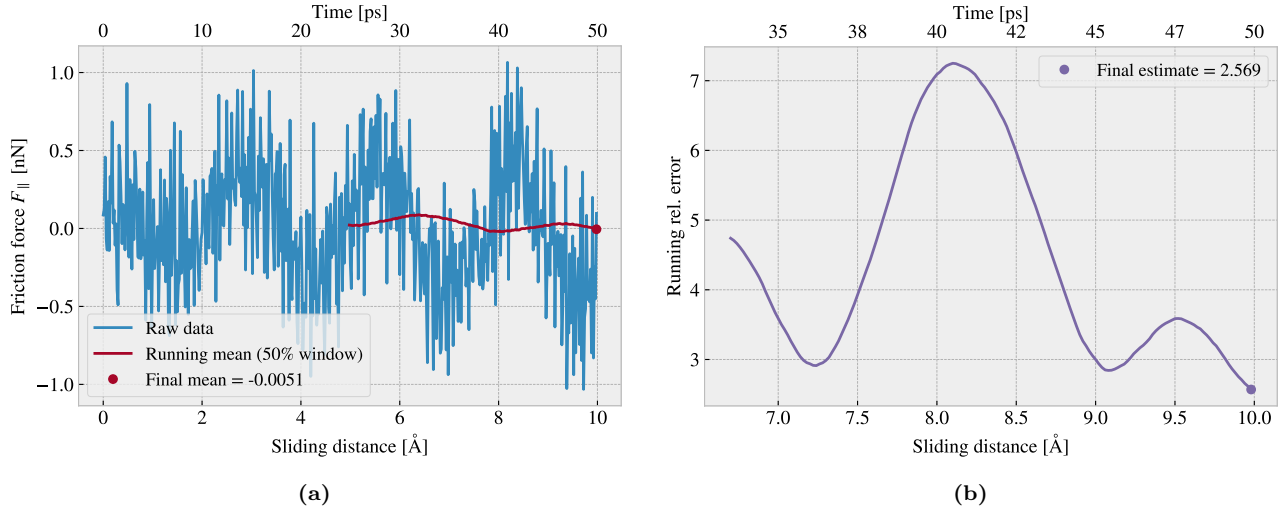


Figure 2.5: Supporting figures for the description of the kinetic friction metric and corresponding uncertainty for an example using a reduced sliding distance of 10 Å. (a) The running mean for the force trace with a window length of 50% of the sliding length in this example. (b) The running relative error calculated using the standard deviation for the 35% running window of the running mean (red line) in panel (a). For both figures, the running value is displayed at the end of their respective corresponding windows.

When including the full dataset of 400 Å of sliding, such that the std window actually matches with the longest period of oscillations expected, we get a final relative error of $\sim 12\%$ as shown in fig Fig. 2.6. This is arguable just at the limit of an acceptable error, but as we shall see later on in Sec. 2.6 this high relative error is mainly associated with the cases of low friction. When investigating different configurations under variation of load and strain we see a considerably lower relative error as the mean friction evaluates to higher values. One interpretation of this finding is that the oscillations in the running mean are not substantially influenced by the

magnitude of the friction. In that case, the relative error will spike for the low friction cases, and the absolute error might be the more reliable measure, i.e. using simply the std without dividing by the final mean value.

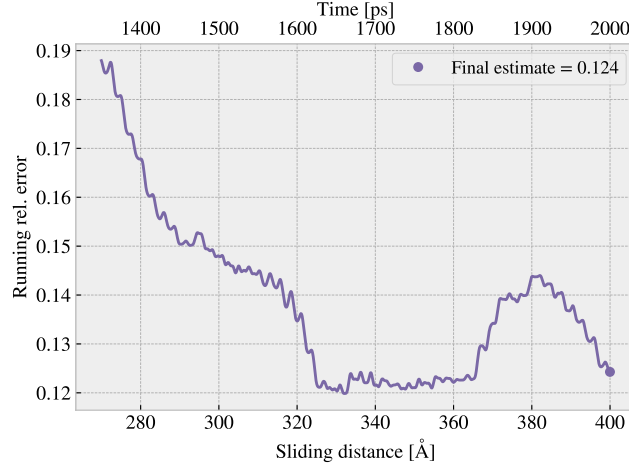


Figure 2.6: Running standard deviation (std) for a full 400 Å sliding simulation. The running std window is 70 Å (35% of the running mean window, which is 50% of the full sliding length).

2.3.2 Static friction

The maximum value is one of the common choices for addressing static friction, even though the definition of static friction is a bit vague. When considering the force traces in Fig. 2.1 we observe that the force oscillations increase in magnitude toward a global peak at ~ 20 Å. Thus, one could be inclined to identify this peak as the maximum value associated with the static friction force. However, as we have already clarified, this steady increase in friction is part of a slower oscillation that repeats with a period of ~ 71 Å. By plotting the top three max values recorded during a full 400 Å simulation, for 30 logarithmically spaced load values in the range $[0.1, 100]$ nN, we observe that the global max rarely falls within this first oscillation period as shown in Fig. 2.7a. Only 2 out of 30 global maxima and 4 out of 90 top three maxima can be associated with the start of the sliding by this definition. Thus, this result suggests that our default system does not yield a static friction response in the sense of an initial increase in friction due to a depinning of the sheet from the static state. Several modifications to the system parameters may enhance the likelihood of observing a substantial static friction response. These include prolonging the initial relaxation time, as static friction is believed to increase logarithmically with time [31], or increasing the sliding force more slowly by utilizing a soft spring tethering. As an attempt to test the latter part of this hypothesis, we conducted a series of simulations with different spring constants, $K \in [5, 200]$ nN, including also $K = \infty$, while maintaining the relaxation period and sliding velocity at their default values. The results shown in 2.7b do not support this hypothesis since the reduction of the spring constant did not lead to the maximum friction peak appearing within the first oscillation period. We acknowledge that this outcome might be compromised by our choice of the relaxation period or sliding speed. However, given the ambiguity surrounding the determination of static friction, we will mainly concern ourselves with kinetic friction in the remainder of this thesis.

2.4 Out-of-plane buckling

The out-of-plane buckling is one of the motivations for investigating the application of Kirigami cuts in the context of friction properties. Therefore, we perform a stretch simulation, at low temperature ($T = 5$ K) without any substrate, in order to verify that we can reproduce an out-of-plane buckling with the Tetrahedron and Honeycomb patterns. For this investigation, we consider the Tetrahedron (7, 5, 1) and the Honeycomb (2, 2, 1, 5) pattern in comparison to the non-cut sheet. We quantify the out-of-plane buckling by assessing the distribution of atoms along the z-direction (perpendicular to the plane) during straining. We calculate the minimum and maximum z-value as well as the atom count quartiles 1%, 10%, 25%, 50% (median), 75%, 90% and 99% as

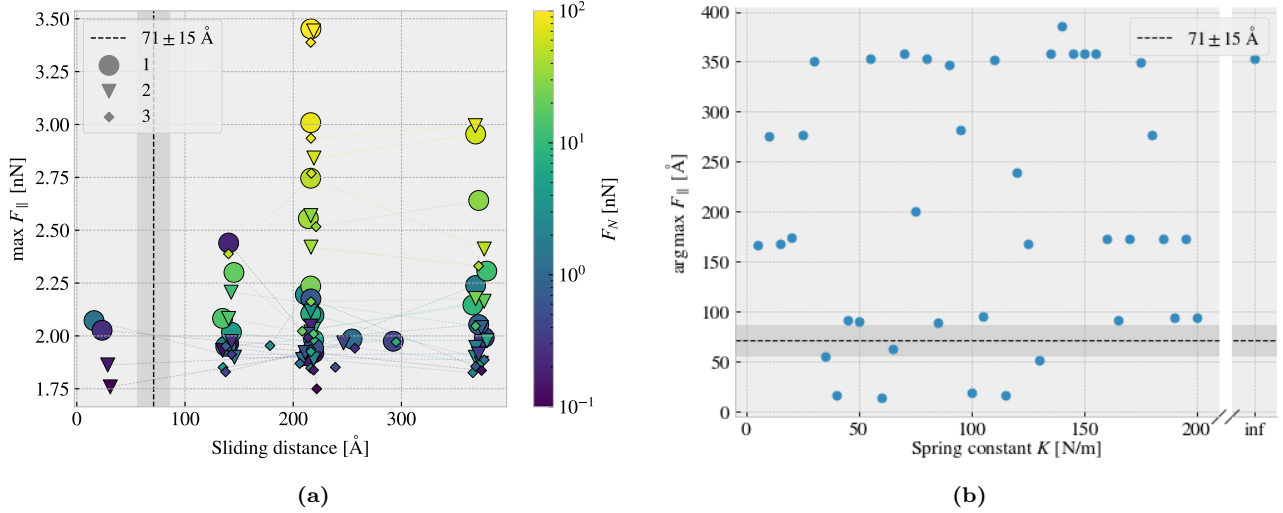


Figure 2.7: Investigation of the sliding displacement corresponding to the maximum friction force peaks. The dotted line, along with the gray-shaded area indicating the degree of uncertainty, represents the slowest significant oscillation period identified in the data. This line serves as a threshold for determining whether a peak falls within the initial portion of the sliding simulation. (a) The top three maxima for simulations with varying loads; 30 logarithmically spaced loads in the range $[0.1, 100]$ nN. The marker shapes denote the top 1, 2 and 3 respectively and the color denotes the normal load. (b) The sliding displacement corresponding to the friction maxima for simulations with varying spring constant; 40 uniformly spaced values in the range $K \in [5, 200]$ N/m in addition to $K = \infty$.

shown in Fig. 2.8. The Tetrahedron and Honeycomb patterns show significant buckling in comparison to the non-cut sheet, which only exhibits minor buckling of ~ 2 Å, which is of the same order as the lattice spacing. We notice that the Tetrahedron pattern buckles more in consideration to the min. and max. peaks while the remaining quantiles seem to be more closely spaced than for the Honeycomb. By addressing the simulation results visually, using the *Open Visualization Tool OVITO*, we find that this can be attributed to fringes on the edge “flapping around” and thus increasing the min. and max. values. This is also evident from the simulation with the substrate seen in ?? in ??.

Given the confirmation of out-of-plane buckling in a vacuum, as seen in Fig. 2.8, we reintroduce the substrate in order to investigate whether this effect carries over to a changing contact area. For this simulation, we raise the temperature to the default value of $T = 300$ K. We keep the normal force off and let the sheet stick purely by the adhesion forces between the sheet and substrate. We quantify the contact area through the relative number of atoms in the sheet within chemical range of the substrate. The cut-off for this interaction is set to 4 Å, adopted from [24], corresponding to $\sim 120\%$ the LJ equilibrium distance. Usually, the contact area is calculated as the number of contacting atoms multiplied by an associated area for each atom. However, since we are not interested in the absolute value of the area, but rather the relative change, we omit the multiplication factor. That is, we consider the relative number of atoms within the contact range as our metric of choice, which is proportional to the contact area. The relative contact for the three configurations (No cut, Tetrahedron (7, 5, 1) and Honeycomb (2, 2, 1, 5)) during straining are shown in Fig. 2.9. The figure reveals a significant drop in relative contact as the sheets are strained, which agrees qualitatively with the buckling observed in Fig. 2.8 without the substrate. The Honeycomb pattern turned out to be both the most stretchable, with a rupture strain of 1.27, and the one with the biggest decrease in relative contact with a minimum of approximately 43%. Notice, that the relative contact is never actual 1.0 but instead reaches a maximum of 96% without strain. This is attributed to the temperature fluctuations and the choice of cut-off.

Selected frames from the simulation result are shown in ?? which reveals a bit more information on how the buckling occurs. The Tetrahedron pattern deforms rather quickly and smoothly into small tetrahedron spikes, as the name suggests. In the Honeycomb pattern, on the other hand, the deformations initiate from one side first. As the sheet stretches more rows of the pattern are activated, producing the honeycomb-looking shape when seen from above. Both patterns exhibit a small increase in relative contact when they are approaching their

yield strain, which agrees with the results from Fig. 2.8 where the buckling reduces slightly towards the rupture strain.

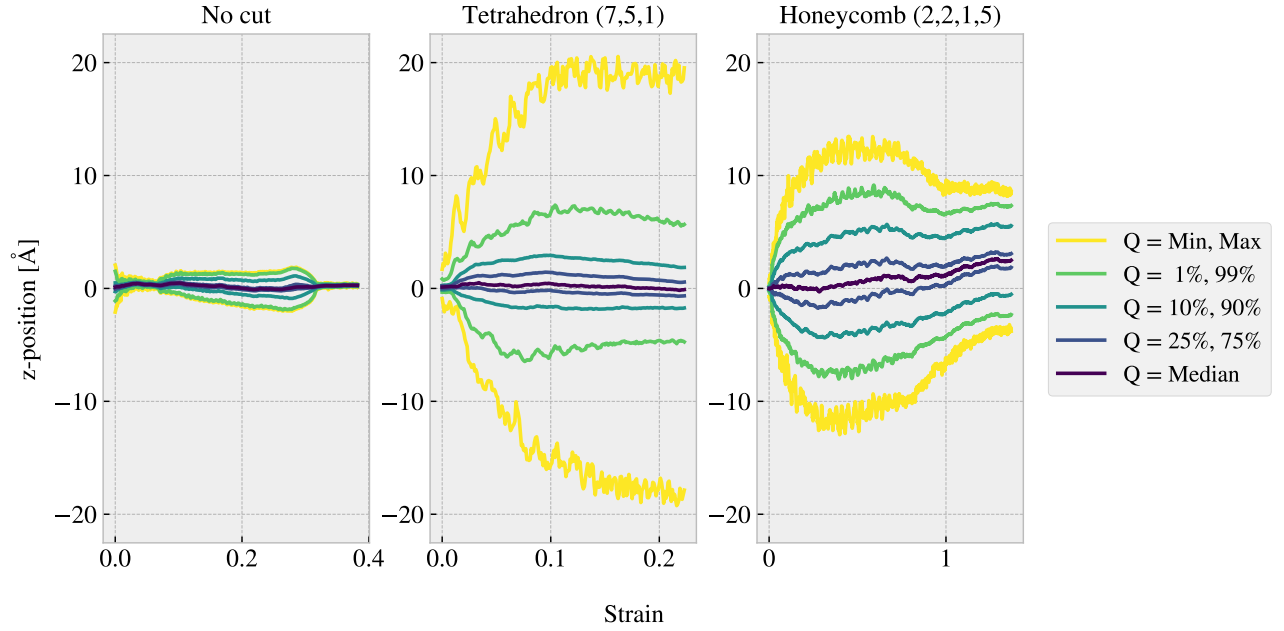


Figure 2.8: The out-of-plane buckling during straining for three different sheet patterns, namely the No cut, Tetrahedron (7, 5, 1), and Honeycomb (2, 2, 1, 5) pattern, in vacuum at low temperature $T = 5$ K. The buckling is quantified by the distribution of the atom z-positions, which are perpendicular to the sheet plane, and the colors indicate selected quantiles. The yield strain for each pattern, from left to right, is 0.38, 0.22, and 1.37, respectively. The results indicate that the Tetrahedron and Honeycomb patterns exhibit significant out-of-plane buckling in comparison to the non-cut sheet.

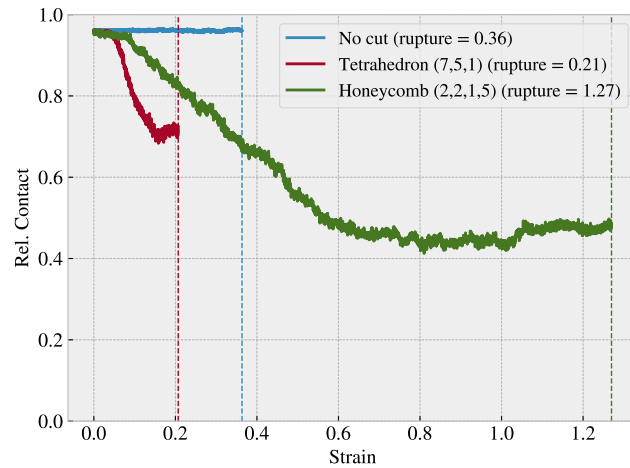


Figure 2.9: Relative contact, given as the relative number of atoms in the sheet being within chemical interaction range, vs. straining of the sheet. The cut-off for the interaction range is 4 \AA corresponding to $\sim 120\%$ the LJ equilibrium distance. No normal force is applied and temperature is kept at $T = 300$ K.

2.5 Investigating default parameters

We carry out a more extensive investigation of the friction dependence on temperature T , sliding speed v_{slide} , spring constant K , and timestep dt . This is done partly to understand how the dependencies relate to the theoretical, numerical and experimental results, and partly to understand how these parameters affect the stability of our system. We use the default parameters presented in Table 2.1 and investigate the results as we change parameters, one at a time. We keep the load at 1 nN. We consider the mean friction force, sampled from the last half of the simulation as described in Sec. 2.3, representing the kinetic friction. The results are shown in Fig. 2.10, where the shaded area (connected linearly) denotes the absolute error defined by the std as described in Sec. 2.3 as well.

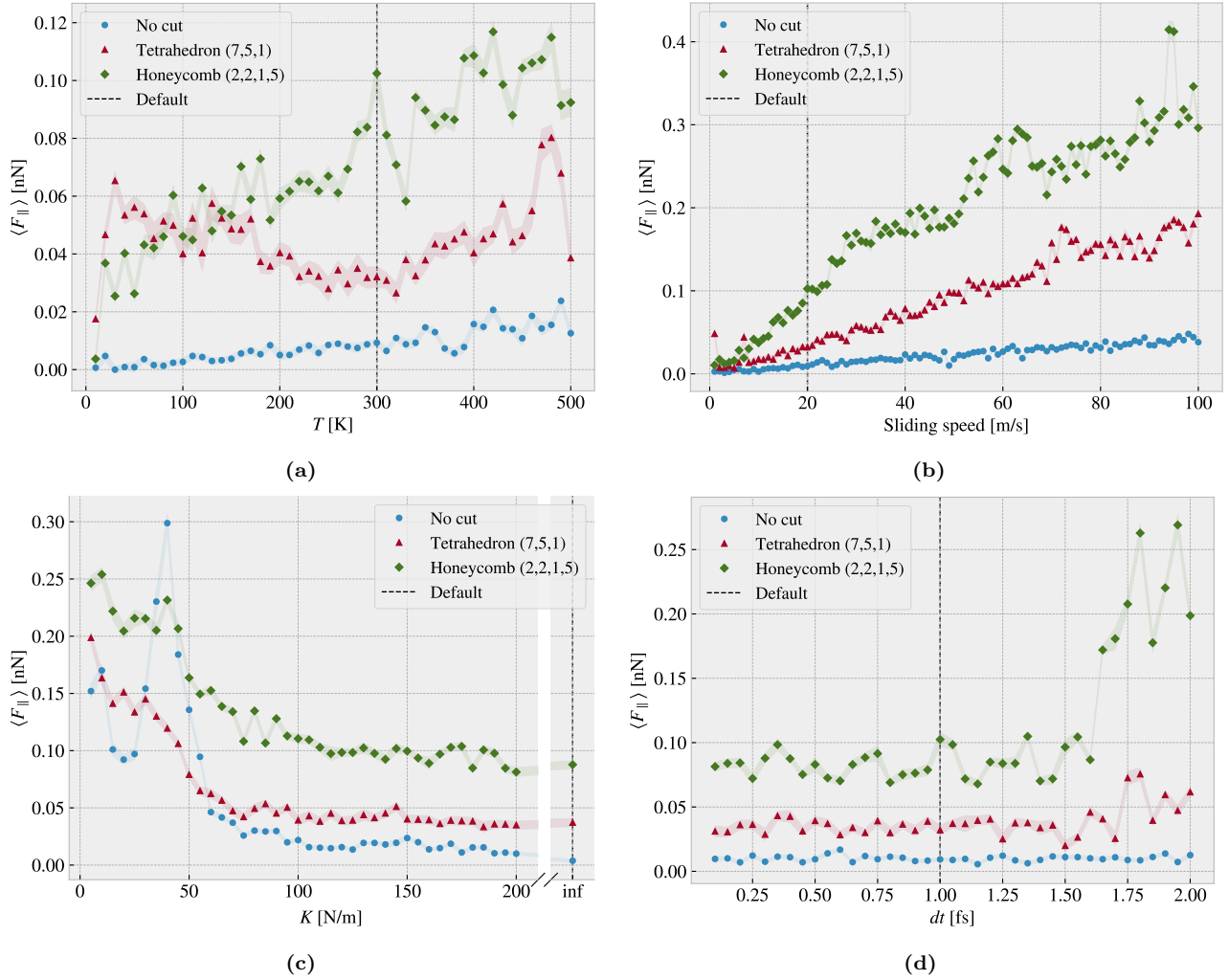


Figure 2.10: Investigation of the friction dependencies to the selected parameters: temperature (a) sliding speed (b), spring constant (c) and timestep (d), the non-cut sheet, non-cut sheet, the Tetrahedron (7, 5, 1), and the Honeycomb (2, 2, 1, 5) patterns. The dotted line denotes the default parameter choice and the shaded area denotes the estimated (\pm) absolute error.

From the temperature investigation in Fig. 2.10a we find an increasing kinetic friction with temperature for both the non-cut sheet and the Honeycomb pattern. The Tetrahedron pattern shows both decreasing and increasing trends. The general trend shows a convex curve in the range (30–480 K) with a minimum around our default choice of 300 K, but with rapid fluctuations at the start (10–30 K) and end region (480–500 K). Similar fluctuations are also seen from the Honeycomb pattern, although it shows an underlying increasing trend throughout. When comparing the non-cut sheet and the Honeycomb pattern we observe that the slope for the increasing trend is higher for the Honeycomb pattern. From the predictions of the Prandtl–Tomlinson model and

experimental results we expect to find a decrease in friction with increasing temperature. However, in similar MD-based studies by Guerra et al. [32] they report that the frictional temperature dependence reverses at high sliding speed. They attribute this to the crossover from the diffusive to the ballistic regime taking place at a sliding speed of 1 to 10 m/s. This agrees with our observations since we are using a sliding speed of 20 m/s. In the absence of any clear suggestions from the results regarding an appropriate temperature, we take the common choice of using the room temperature 300 K. The non-cut and Tetrahedron friction shows to be rather stable around our temperature of choice, although we do see some significant fluctuations for the Honeycomb pattern in this range. However, we do not regard this as a critical feature.

From the sliding speed investigation in Fig. 2.10b we generally find increasing friction with velocity. Due to the relatively high velocities used in these simulations, we expect a viscous friction $F_k \propto v_{\text{sliding}}$ as reported by Guerra et al. [32] and predicted by the Prandtl–Tomlinson model. In general, this aligns rather well with our results, especially for the non-cut sheet. However, the Tetrahedron and Honeycomb sheets seem to fall slightly into a sublinear relationship as it approaches higher velocities. This behavior could potentially be attributed to velocity saturation, a phenomenon predicted by the Prandtl–Tomlinson model without considering the damping effect of the thermostat. On the other hand, experimental results generally show a logarithmic increase in friction with velocity, which may align better with the behavior observed for the Tetrahedron pattern. Furthermore, we find that the Tetrahedron and Honeycomb patterns both display indications of local fluctuations that could be attributed to phonon resonance effects, as discussed in relation to the Frenkel-Kontorova models. Our choice of a sliding speed at 20 m/s mainly reflects a consideration of computational cost, but the fact that no immediate resonance fluctuations appear in the proximity of this value supports the choice further.

From the investigation of the spring constant parameter in Fig. 2.10c we observe a significant decrease in friction as the springs stiffen. This can be attributed to the transition from a stick-slip influenced regime to a smooth sliding regime as evidenced by the force traces in Fig. 2.1. For soft springs the friction response is quite sensitive to the specific choice of spring constant which is especially seen for the non-cut sheet around $K = 40$ N/m. Thus, in order to avoid this domain we settled for the infinitely stiff spring. This is also considered a more favorable option due to its ability to provide greater standardization of the simulations since it allows for a more controlled movement of the sheet.

Finally, we consider the numerical stability of the simulation result as we vary the simulation timestep in Fig. 2.10d. The results indicate that the simulation is generally stable below a timestep of ~ 1.5 fs, beyond which instability arises for the cut sheets (Tetrahedron and Honeycomb). This confirms that our choice of timestep is reasonable, but we do observe some fluctuations that are more pronounced for the cut sheets. These fluctuations imply that randomness plays a role in our simulations and that the cut sheets exhibit relatively higher instability compared to the non-cut sheet. Further investigation through varying the random seed for the initial velocity and thermostat could shed more light on this matter. In the meantime, we may consider these fluctuations as a sign that the uncertainty in our results is higher than our estimation from using the running mean and running std. For the Honeycomb sheet, these fluctuations are on the order of ± 0.017 nN.

2.5.1 Computational cost

Our simulations are carried out on a CPU cluster made available by the University of Oslo. This allows us to run multiple simulations at once and with each simulation running in parallel on multiple CPU cores as well. When selecting the simulation parameters, we also need to keep in mind the computational cost. Given that the chosen parameters will be applied to multiple simulations, any increase in computational time will be multiplied by the number of intended simulations, which is roughly 10,000. The computational cost is especially dependent on the timestep and the sliding speed as this will affect the number of computations. As an extension of the analysis in Sec. 2.5 we report on the computational times associated with temperature, sliding speed, spring constant and timestep. By retrieving the computational time used for the parameter investigation in Fig. 2.10 we get the timing shown in Fig. 2.11. Note that these timings are only based on a single simulation for each parameter as opposed to an average over multiple runs which is necessary for more reliable data.

The computational time is governed by the number of timesteps in the simulation and the time used per timestep. For a fixed sliding distance, the number of timesteps in the simulation is inversely proportional to sliding speed and similar inversely proportional to timestep dt . From the results in Fig. 2.11 we find that the sliding speed obeys this expectation rather well by $t \propto v^{-0.977 \pm 0.005}$. The timing did not increase as strongly as expected for the timestep, falling below the $1/dt$ relation with $t \propto dt^{-0.87 \pm 0.02}$. Moreover, we find that increasing temperature also makes for an increased computation time. This can be attributed to an increase

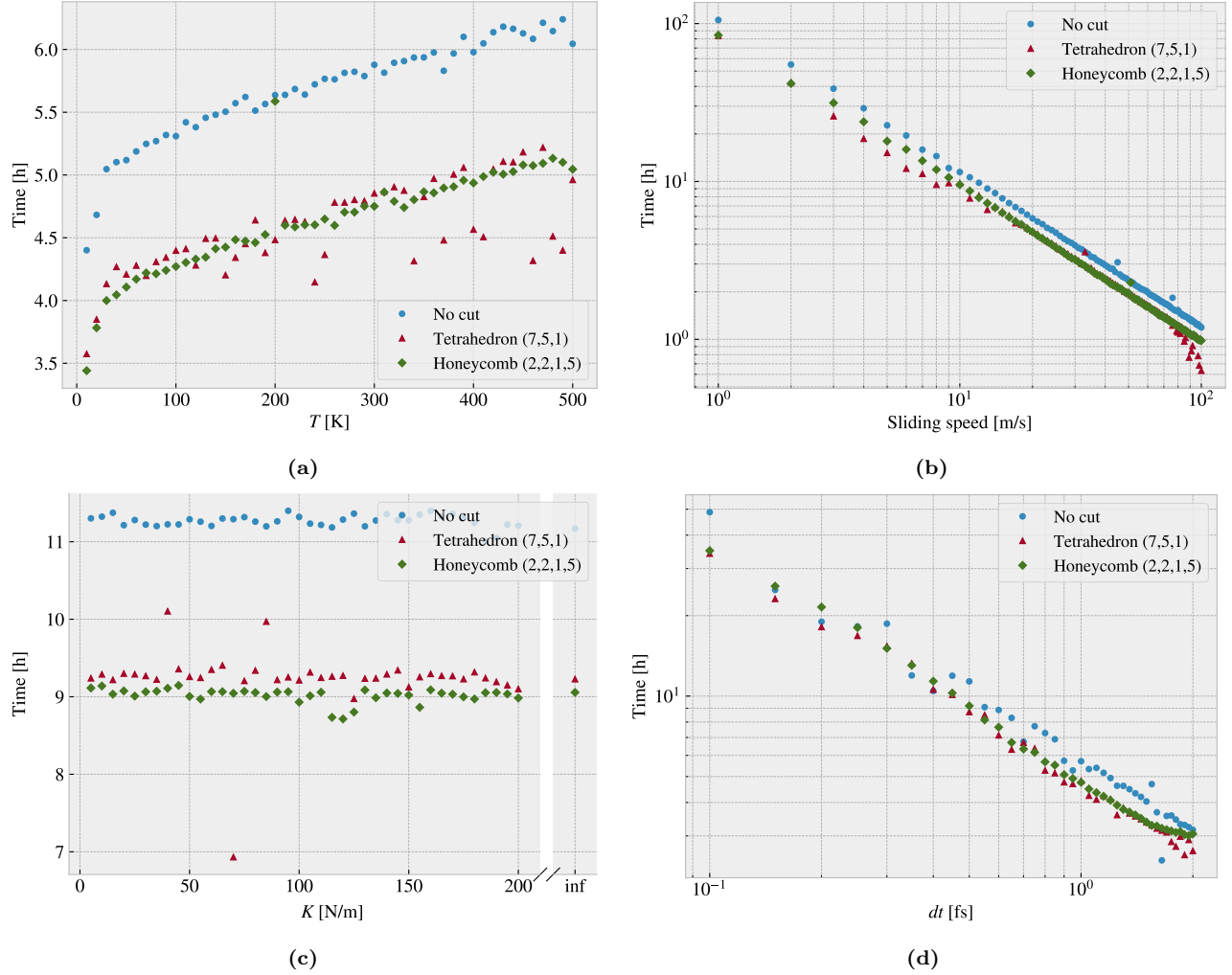


Figure 2.11: The computational cost related to the parameter choice of temperature, sliding speed, spring constant and timestep, in terms of CPU hours running on 16 cores on the CPU cluster. The timing of the sliding speed is found to $t \propto v^{-0.977 \pm 0.005}$ while the timing for the timestep follows $t \propto dt^{-0.87 \pm 0.02}$.

in the computation time associated with the force calculations. The rising temperature gives rise to more fluctuations in the system which might yield more atoms within the force calculation cutoffs for each computation. This kind of consideration can also be attributed to the reason for the deviating timing for dt . Finally, for the spring parameter, we did not see any noticeable effect on timing.

In general, we have selected our simulation parameters: temperature, sliding speed, spring constant, and timestep, based on numerical stability and computational cost. For the timestep, we found that a value of 1 fs, commonly used in similar studies [26, 27], produced stable results while higher values were prone to instabilities and lower values were computationally expensive. The sliding speed was chosen primarily based on computational cost, with a default value of 20 m/s being a reasonable compromise between computational efficiency and relatability to the lower values more commonly used in other studies. Although a lower sliding speed could lead to an interesting regime governed by stick-slip motion, it represents a factor of 20 increase in computational time. Since stick-slip motion is out of reach based on the chosen sliding speed, we found that using an infinitely stiff spring $K = \infty$ was the most reasonable option to ensure stable results. Finally, the temperature investigation did not provide much guidance for a specific choice, so we settled for the standard choice of room temperature $T = 300$ K.

2.6 Load and stretch dependencies

So far, we have carried out a general analysis of the system behavior under the influence of various simulation parameters. This lays the foundation for the remaining study as we now shift our intention towards the friction dependence of strain and load.

2.6.1 Pressure reference for normal load

We consider a load range of 0.1–10 nN which coincides with the general investigated range in other MD studies [24, 27]. In order to relate the magnitude of this load we provide a short calculation of the corresponding pressure. We will use the pressure underneath a stiletto-heeled shoe as a high-pressure reference from a macroscale perspective. The diameter of a stiletto-heeled shoe can be less than 1 cm [33], and hence an 80 kg man³ standing on one stiletto heel, with all the weight on the heel, will generate a pressure

$$P = \frac{F}{A} = \frac{mg}{r^2\pi} = \frac{80 \text{ kg} \cdot 9.8 \frac{\text{m}}{\text{s}^2}}{\left(\frac{10^{-2} \text{ m}}{2}\right)^2 \pi} = 9.98 \text{ MPa}.$$

The fact that the pressure under a stiletto heel can get this high, actually greater than the pressure under an elephant foot, is an interesting realization in itself that is often used in introductory physics courses [34]. Nonetheless, this serves as a reasonable upper bound for human executed pressure. With a full sheet area of $\sim 212 \text{ nm}^2$ our load range of 0.1–10 nN corresponds to a pressure of 0.47–47 MPa which relates reasonably to our macroscale reference. This pressure might be incompatible with various industrial purposes, but with no specific application in mind, this serves as a decent reference point. Notice, that if we consider a human foot with the area 113 cm^2 [35] the pressure drops to a mere 70 kPa corresponding to only $\sim 0.01 \text{ nN}$.

2.6.2 Strain dependency

We consider the effects of stretching the sheet using the non-cut, Tetrahedron (7, 5, 1) and Honeycomb (2, 2, 1, 5) sheet as used so far. While we consider the actions of “stretching” and “straining” to be synonyms we will describe the sheet deformation state with the technical term *strain*. The strain describes the change in length relative to a reference length. We use the relaxed sheet as our reference length L_0 for which the straining towards a length L corresponds to the strain $\epsilon = (L - L_0)/L_0$. Thus a strain of 0 corresponds to the relaxed sheet and a strain of 1 corresponds to a doubling of sheet length. Notice that the measure of strain is dimension specific, but we will only consider the y-direction which corresponds to the direction of applied strain in the simulations. For each configuration, we run a rupture test where the given sheet is stretched under zero load, but still under the influence of adhesion from the substrate. The rupture strain is then recorded, and multiple new simulations are initiated with strain values uniformly spaced between zero and the rupture strain. First, we aim to reproduce the contact investigation from Fig. 2.9. We quantify the relative contact as described in Sec. 2.4, but we convert this into a single metric for a given simulation by considering the mean of the last 50% of the data points, similar to what we have done for the mean friction. We also adopt a similar method for quantifying the error (see Sec. 2.3). Fig. 2.12a shows a significant decrease in relative contact with strain for the kirigami patterns. This agrees qualitatively with the non-loaded continuous strain simulations in Fig. 2.9. This result implies that the change in contact is not governed by a momentum effect during stretching, as each simulation now keeps a constant strain throughout. From an asperity theory point of view, the reduction in contact area is theorized to induce a linearly dependent reduction in friction. However, when considering the kinetic friction in Fig. 2.12b we find that this is not the case. For the Tetrahedron and Honeycomb patterns, we find that the friction initially increases with a decreasing contact area. Yet, these are not simply inversely proportional as the friction force suddenly dips down and up again, in the strain range of 0.08–0.11 for the Tetrahedron and 0.73–1.05 for the Honeycomb pattern. When considering the non-cut sheet, we find that both the contact area and friction remain seemingly unaffected by strain. This indicates that the contact area is not a dominating mechanism for friction in our system, although the non-linear friction-strain curve might be correlated with a decrease in contact area through an underlying mechanism related to the out-of-plane buckling. This can be supported by the fact that the contact-strain and friction-strain curves for the Honeycomb pattern both show signs of a discontinuous jump around a strain of 0.32.

³Yes, a man can certainly wear stiletto heels.

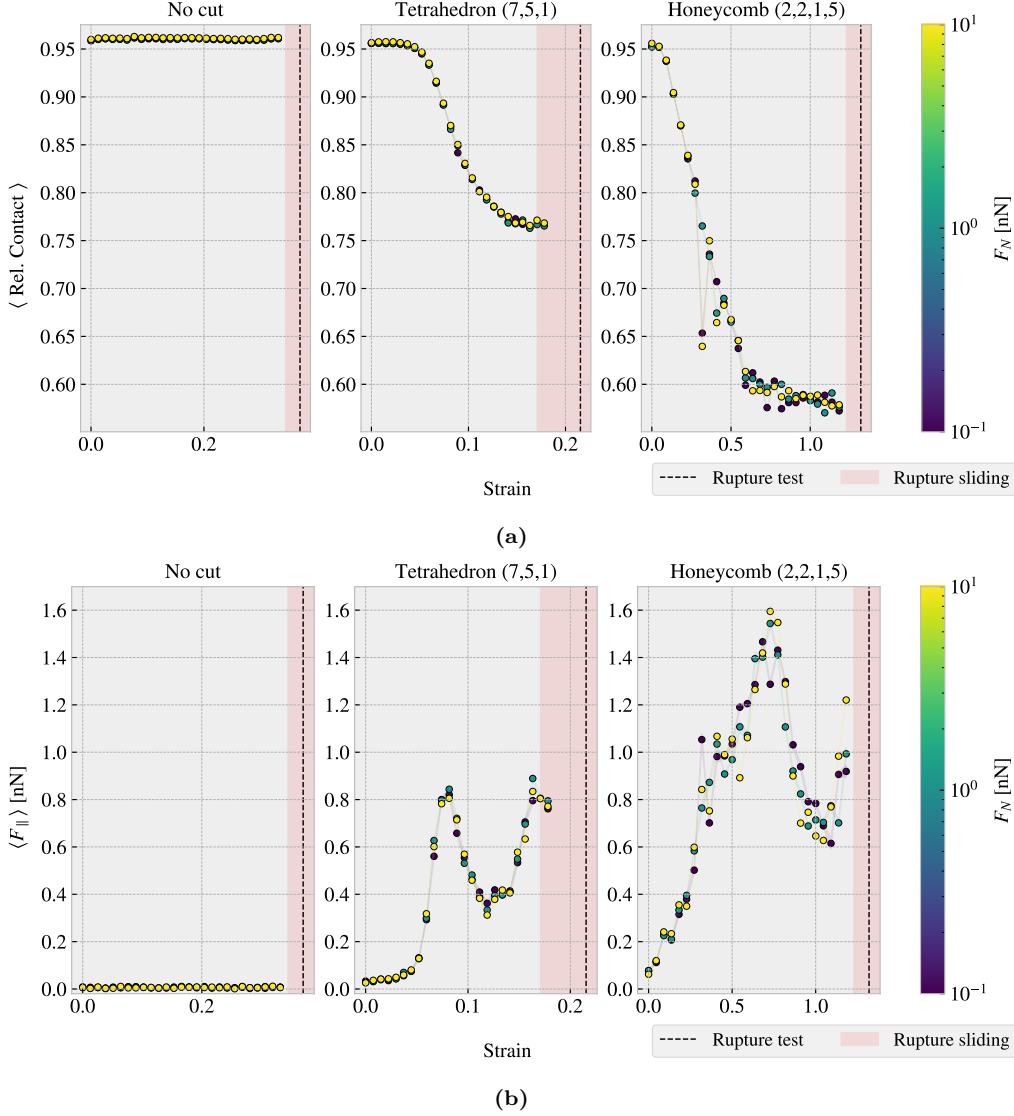


Figure 2.12: Investigation of the frictional behavior for the non-cut, Tetrahedron (7, 5, 1) and Honeycomb (2, 2, 1, 5) sheet under varying strain, consisting of 30 strain values uniformly spaced between 0 and the rupture strain in combination with loads 0.1, 1 and 10 nN. The shaded area, connecting the dots linearly, denotes the the absolute error. The red shade denotes the strain range where ruptures occurred during sliding while the black-dotted line represents the rupture point in the non-loaded rupture test. (a) The average relative contact defined as the relative number of atoms within a contact threshold of 4 Å to the substrate. The absolute error is generally on the order 10^{-4} . (b) The average mean friction force. The absolute error is generally on the order 10^{-3} nN.

Since the non-cut sheet exhibits a flat friction-strain profile we cannot attribute the behavior to an increased tension either. Zhang et al. [30] reported that the friction for a graphene sheet decreases with tension which qualitatively contradicts our observation and supports that tension is not a governing mechanism. Instead, we might attribute the results to a commensurability effect which is predicted by the Frenkel-Kontorov models and observed in both numerical and experimental studies, or perhaps a change in the structural stiffness which is reported as an important feature by [36].

We notice that the initial friction value of the non-strained sheet varies among different configurations, with the non-cut sheet exhibiting the lowest initial friction value ($\sim 7 \times 10^{-4}$ nN), the Tetrahedron sheet having a slightly higher value (~ 0.03 nN), and the Honeycomb sheet exhibiting the highest (~ 0.07 nN). This is more clearly shown in the parameter investigation in Fig. 2.10. This supports the idea of a commensurability effect as the removal of atoms might affect the lattice structure of the sheet slightly. However, the magnitude of this

effect is generally one order of magnitude lower than the strain-induced friction effect. We attribute this to the idea that the reorganization of the contacting atoms has significantly more impact on commensurability than removing some atoms from the lattice. We notice also that the two orders of magnitude increase in normal load did not make a significant difference in the results. The estimated absolute error marked by a shaded area in Fig. 2.12b were fairly low for both friction on the order 10^{-3} nN and relative contact on the order of 10^{-4} .

By considering the increase in friction from zero strain towards the first peak of the friction-strain curve we find that the Tetrahedron pattern exhibits a relative friction increase of ~ 27.7 while the Honeycomb pattern exhibits a relative increase of ~ 22.4 . This is in itself an interesting result, but considering that the friction drops almost as dramatically afterward is even more unexpected. For the Tetrahedron pattern, the friction drops by ~ 0.51 nN during an increased strain $\Delta\epsilon \sim 0.04$ while for the Honeycomb pattern the friction drops ~ 0.98 nN during a strain increase of $\Delta\epsilon \sim 0.36$. These results are promising for the aim of achieving a negative friction coefficient for a system with coupled load and strain. We will discuss this further at the end of this chapter in Sec. 2.6.4.

2.6.3 Load dependency

From the investigation of the strain dependency we saw that increasing the normal load from 0.1 to 10 nN did not make a considerable impact on the friction in comparison to the effect associated with strain. One special feature of our system is that we only apply load to the pull blocks, and thus we might suspect this to be of importance. Therefore, we investigate the friction under varying loads for a non-cut sheet comparing the case of loading only the pull blocks against a uniform loading of the entire sheet as shown in Fig. 2.13. Both load distributions show a seemingly non-dependent relationship between friction and load considering the size of our estimated error. Thus, we do not find any indications that the uniform loading changes the qualitative behavior of our system.

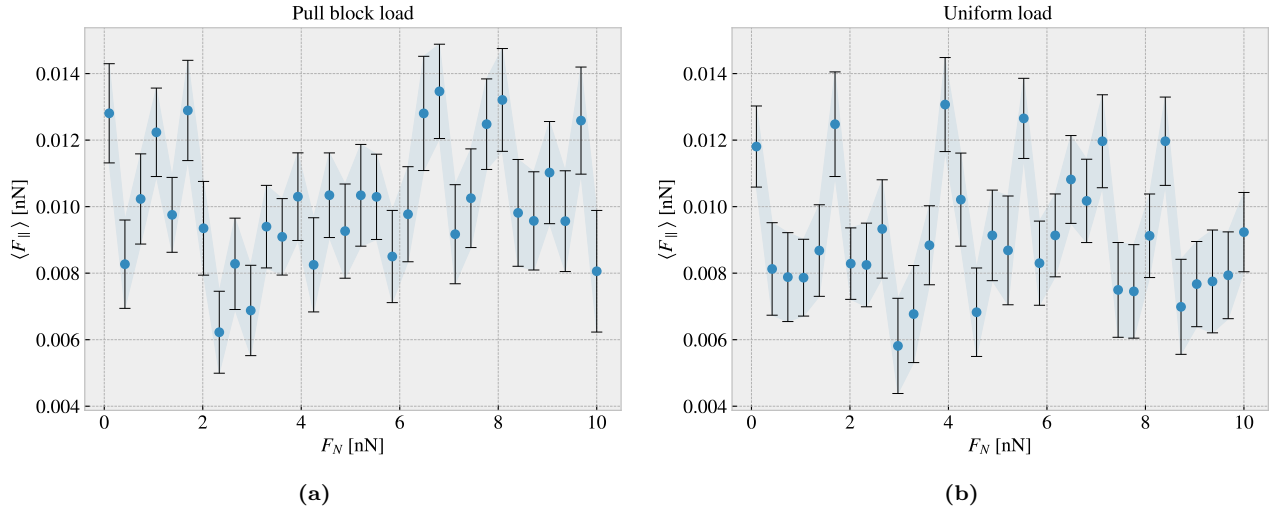


Figure 2.13: Multiple simulations of a non-cut sheet under various uniformly spaced load values $F_N \in [0.1, 10]$ nN for two different variations of loading distribution. The shading and the error bars denote the absolute error. (a) The loading is applied to the pull blocks only. (b) The loading is applied uniformly to the full sheet.

To examine the relationship between friction and normal load as the Kirigami patterns undergo strain, we conduct additional simulations with logarithmically spaced normal loads in the range of 0.1 to 100 nN. This is done for a selected subset of strain stages from Fig. 2.12b, with 30 load data points for each strain. We also monitor the relative contact during the increased load. The results are shown in Fig. 2.14. From Fig. 2.14b we observe that three orders of magnitude load increase yields a small increase in friction for all Kirigami patterns. This effect is more pronounced in the figure for the non-cut sheet, but this is mainly because the friction axis shows a narrower range for this figure. It should be noted that due to the logarithmic scale of the load axis, any apparent linear trends in the figure are in fact sublinear. Nonetheless, as the normal load approaches 100 nN, there is some indication of an increase in friction reminiscent of a linear relationship. However, it is difficult to

draw firm conclusions as the magnitude of the increase in friction is relatively small compared to the level of noise in the data.

For the investigation of contact area in Fig. 2.14a, we generally find an increasing contact area with load. By considering the full load from 0.1 nN to 100 nN we find the largest increase in relative contact, among the various values of relative strain, to be 0.007 for the non-cut, 0.014 for the Tetrahedron and 0.025 for the Honeycomb sheet. This constitutes a rather small change and thus it is difficult to assess how this relates to a dependency between the contact area and the friction. However, we do see that the Tetrahedron and Honeycomb patterns exhibit a larger change in contact area which aligns with the idea that the out-of-plane buckling makes them behave more like an asperity system. When plotting friction against relative contact in Fig. 2.14c we do not find any significant evidence for a linear relationship between contact area and friction as otherwise proposed by asperity theory. Instead, from the Tetrahedron and Honeycomb pattern, we confirm that the strain-induced effects are dominant in comparison to any effects from the contact area. By studying an even larger load range we might get more insight into this relationship. Note that we have omitted the error bars in Fig. 2.14 for visual purposes, but the absolute errors for both the relative contact and friction are on the same order of magnitude as shown in both Fig. 2.12 and Fig. 2.13.

From the friction measurements in Fig. 2.14b we find that the non-cut sheet generally produces a friction force in the order of 0.005–0.0025 nN throughout the 0.1–100 nN load range. Using a ratio based friction coefficient definition ??, $\mu_1 = F_{\text{fric}}/F_N$, this would lead to a coefficient roughly in the range

$$\mu_1, \text{ ??}: \quad \text{No cut} \sim [10^{-4}, 0.13], \quad \text{Tetrahedron} \sim [4 \times 10^{-4}, 8.7], \quad \text{Honeycomb} \sim [9 \times 10^{-4}, 15.2].$$

However, these values mainly reflect the poorness of this definition, as we find the values to diverge at low load and decrease towards high load due to the lacking linear relationship and an offset in the load curve corresponding to a finite friction at zero load. This offset is drastically enhanced for the Kirigami patterns under strain. Due to the small changes in friction compared to the noise in the data, it is not sensible to calculate the slope dF_{fric}/dF_N as a function of load. Nonetheless, if we force a linear fit for the whole range and use the second definition ?? as $\langle \mu_2 \rangle = \Delta F_{\text{fric}}/\Delta F_N$, we get average coefficients in the range

$$\mu_2, \text{ ??}: \quad \text{No cut} \sim [4, 9] \times 10^{-5}, \quad \text{Tetrahedron} \sim 5 \times [10^{-5}, 10^{-4}], \quad \text{Honeycomb} \sim [1, 9] \times 10^{-4},$$

depending on the strain values. These numbers should be interpreted cautiously, but we can take it as a rough estimate of the friction coefficient being on the order 10^{-4} – 10^{-5} . This relates to the finding by [37] who reported a seemingly non-existing relationship between friction and normal load for a graphene sheet with changes in friction that corresponds to friction coefficients in the range 10^{-3} – 10^{-4} when using the slope definition ??. This supports the idea that the graphene sheet does exhibit superlubric behavior in these conditions and that the initial non-strained sheet is in an incommensurable configuration. Thus any strain-induced effects might introduce a more commensurable configuration. This aligns with the observed increase in friction and the fact that the friction never gets smaller than the initial friction value. The non-linear effects can then be attributed to transitions in and out of commensurable phases. The observation that the friction dependency on load is relatively unaffected by the straining suggests that the strain-induced effects are independent of any load-related effects on friction. That is, the introduction of strain mainly shifts the friction-load curve but does not significantly alter its slope.

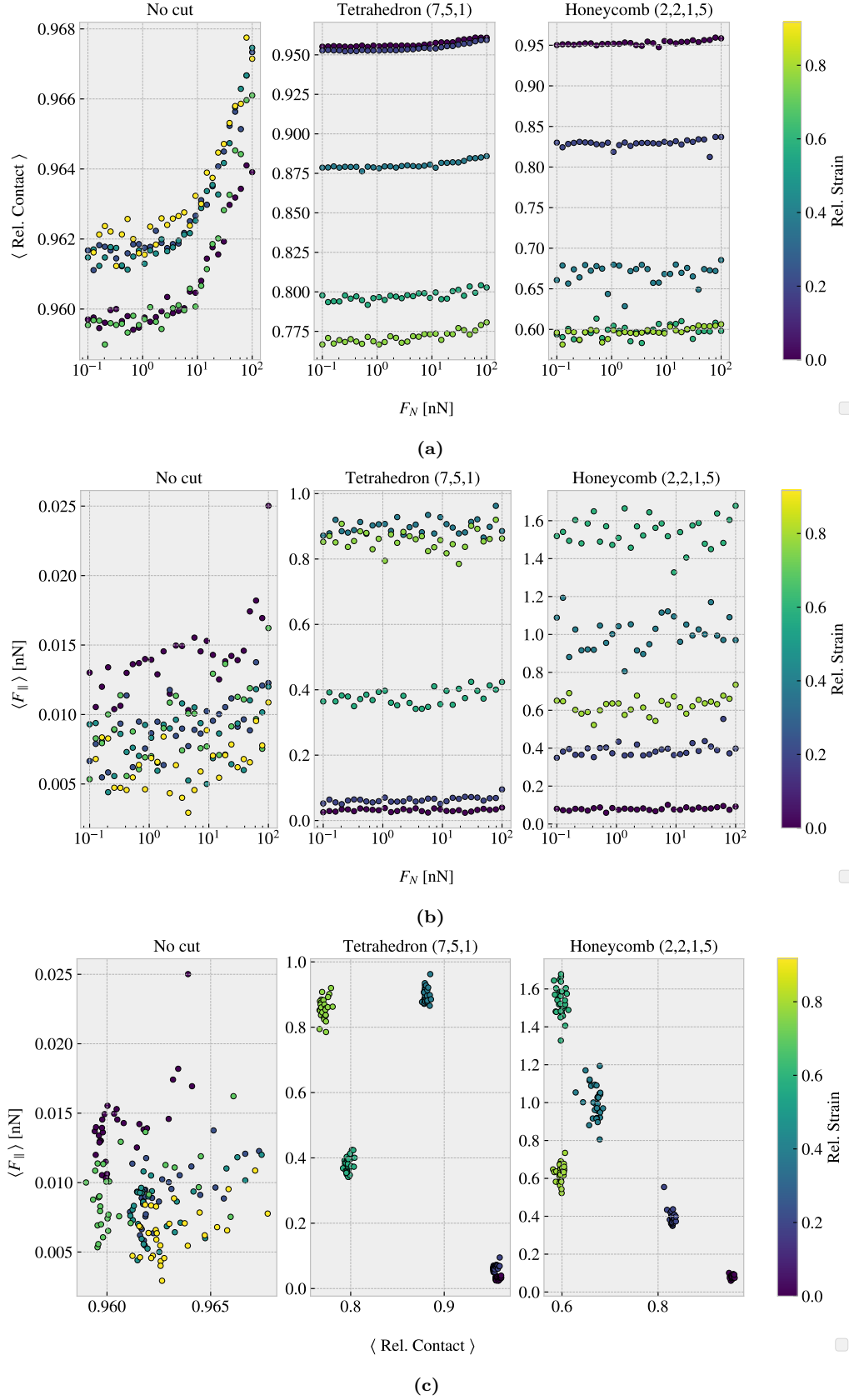


Figure 2.14: Investigation of the frictional behavior for the non-cut, Tetrahedron (7, 5, 1) and Honeycomb (2, 2, 1, 5) sheet under varying load, consisting of 30 logarithmically spaced load values in the range 0.1–100 nN, at different strain stages relative to their rupture strains. (a) The average relative contact. (b) The average mean friction. We omitted the indication of the absolute errors as they were similarly low as seen in Fig. 2.12. (c)

2.6.4 Prospects of a negative friction coefficient

Considering the results from Sec. 2.6.2 and Sec. 2.6.3 we find that strain-induced friction effects, on the order of $/SI1nN$, are generally dominating in comparison to load-induced effects on the order of 0.01 nN given a load range of 10^2 nN . This is promising for the idea of achieving a negative friction coefficient for a nanomachine system that couples load and strain. By applying load on the nanomachine we would increase both the load and the strain on the sheet simultaneously. However, since the friction dependency to strain dominates in comparison to load effects such a system can in practice be designed entirely by considering the strain dependency. The friction coefficient is by our definition (??) given as the slope of the friction F_f vs. normal force F_N curve. Hence, for two points $\{(F_{N,1}, F_{f,1}), (F_{N,2}, F_{f,2})\}$, $F_{N,1} < F_{N,2}$ we can evaluate the associated friction coefficient $\mu_{1,2}$ as

$$\mu_{1,2} = \frac{F_{f,2} - F_{f,1}}{F_{N,2} - F_{N,1}} = \frac{\Delta F_f}{\Delta F_N}.$$

If we neglect load effects, $F_f(F_N, \varepsilon) \sim F_f(\varepsilon)$, and consider a load-strain coupling $\varepsilon = RF_N$ with linear coupling ratio R we get

$$\mu_{1,2}(\varepsilon_1, \varepsilon_2) = \frac{\Delta F_f(\varepsilon_1, \varepsilon_2)}{\frac{1}{R}(\varepsilon_2 - \varepsilon_1)} = R \frac{\Delta F_f(\varepsilon_1, \varepsilon_2)}{\Delta \varepsilon}. \quad (2.1)$$

When considering the ratios $\Delta F_f / \Delta \varepsilon$ for the reduction in friction with strain for the Tetrahedron and Honeycomb patterns in Sec. 2.6.2 we find the corresponding coupled system friction coefficients to be

$$\text{Tetrahedron: } R \frac{-0.51\text{ nN}}{0.04} = -R \cdot 12.75\text{ nN}, \quad \text{Honeycomb: } R \frac{-0.98\text{ nN}}{0.36} = -R \cdot 2.72\text{ nN}. \quad (2.2)$$

This showcases that we might be able to utilize the strain effect to achieve a negative friction coefficient for the system of coupled strain and load. This is investigated further in ??.

Chapter 3

Summary

In this thesis, we have studied the nanoscale friction of a Kirigami graphene sheet under the influence of load and strain using MD simulations. We have developed a numerical framework for generating diverse Kirigami designs which we have utilized to create a dataset for the frictional behavior depending on Kirigami pattern, strain, and loading. Our findings suggest that the frictional behavior of a Kirigami sheet is highly dependent on the geometry of the pattern and the strain conditions. We observed that the out-of-plane buckling can be associated with a non-linear friction-strain curve which can be utilized to demonstrate a negative friction coefficient in a system with coupled load and strain. Moreover, we have investigated the possibility to use machine learning on this dataset and attempted an accelerated search. Our findings imply that machine learning can be feasible for this approach, additional data is required to establish a more reliable foundation for a search for new Kirigami patterns. In this chapter, we will provide a summary of our findings and draw conclusions based on the results obtained. Finally, we will suggest some topics for further research.

3.1 Summary and conclusions

3.1.1 Designing an MD simulation

We have designed an MD simulation for the examination of friction for a graphene sheet sliding on a silicon substrate. The key system features were the introduction of the pull blocks, defined as the end regions of the sheet with respect to the sliding direction, which was utilized for applying normal load and sliding the sheet. The pull blocks were made partly rigid and used to employ a thermostat as well. Through an analysis of the friction forces retrieved from sliding simulations, we have established a standardized metric for kinetic friction. In particular, we measured the force exerted by the substrate on the full sheet, including the pull blocks, with respect to the sliding direction, and determined the kinetic friction as the mean value of the last half of the simulation. The uncertainties were estimated based on the fluctuations in the running mean. We found that the assessment of static friction was ambiguous for our simulation and did not pursue this further. From the analysis of the force traces, friction force vs. time, we identify the friction behavior in our simulation domain as being in the smooth sliding regime. This is attributed to the choice of a relatively high sliding speed (20 m/s) and infinitely stiff springs for the tethering of the sheet. This was supported by a demonstration of a transition to the stick-slip regime through the use of softer springs and a decrease in sliding speed. By conducting a more systematic investigation of the effects of temperature, sliding speed, spring constant and timestep, we identified a set of default values based on numerical stability and computational cost. During this process, we aimed to select the variables that would maintain a relatively stable measured friction with moderate perturbations around these default values. We found that friction increased with temperature which we attribute to being in the ballistic sliding regime. In the absence of clear indications from the investigation regarding an appropriate temperature, we opted for the standard choice of room temperature, 300 K. Furthermore, we found friction to increase with velocity as expected, with some signs of phonon resonance at certain sliding speeds as well. We chose a rather high velocity of 20 m/s mainly for the consideration of computational costs. For the spring constant, we found decreasing friction with increasing stiffness of the springs. This is associated with the transition from a stick-slip-influenced regime toward smooth sliding and can be attributed to an underlying change in commensurability. The choice of an infinitely stiff spring was made from an assessment of the variation

in friction with perturbations in the spring constant value. Finally, we confirmed that a timestep of 1 fs provides reasonable numerical stability. However, based on fluctuations with timestep we find that the uncertainty in the simulations might be higher than first estimated. For the non-strained Kirigami sheet, these fluctuations were on the order of ± 0.017 nN for the evaluation of the kinetic friction.

3.1.2 Generetig Kirigami patterns

In order to investigate the effects of Kirigami design we have created a numerical framework for generating various patterns. By defining an indexing system for the hexagonal lattice structure we were able to define the Kirigami designs as a 2D binary matrix for numerical implementation. We have selected two macroscale designs, which we denote the *Tetrahedron* and *Honeycomb* patterns, based on their ability to exhibit out-of-plane buckling when subjected to strain. By digitalizing the designs to match the hexagonal graphene lattice, we found that the characteristic design features can be translated to the nanoscale, as we observed similar out-of-plane buckling in MD simulations. Through our numerical framework we were able to create an ensemble of perturbed unique variations which yielded approximately 135×10^3 and 2.025×10^6 unique configurations for the Tetrahedron and Honeycomb patterns respectively. When considering the possibility to translate the periodic patterns on the graphene sheet the number of possible patterns can be increased by approximately a factor of 100. To introduce some random design features, we have developed a framework for generating Kirigami patterns based on random walks. The framework includes mechanisms such as bias, avoidance of existing cuts, preference for maintaining a direction, and procedures for repairing the sheet for simulation purposes. In general, we found that the capabilities of this numerical framework for generating Kirigami designs exceeded our computational resources with regard to performing MD simulation under different loads and strains for each of the designs. In general, we found that the computational capacity of our numerical framework for generating Kirigami designs surpassed our available resources for conducting MD simulations under various load and strain for each design. Our MD-based dataset only utilized a subset of configurations with 9660 data points based on 216 Kirigami configurations (Tetrahedron: 68, Honeycomb: 45, Random walk: 100, Pilot study: 3). Hence, we argue that the Kirigami generative framework can be valuable for further studies on an extended dataset.

3.1.3 Control friction using Kirigami

We have investigated the frictional behavior of the Tetrahedron and Honeycomb patterns in comparison to a non-cut sheet under various strains and loads. Initially, we observed that straining the Kirigami sheets in a vacuum resulted in an out-of-plane buckling. When adding the substrate to the simulation this translated into a decreasing contact area with strain. We found the Honeycomb sheet to exhibit the most significant buckling with a corresponding reduction of relative contact area to approximately 43%, whereas the non-cut sheet did not produce any significant buckling in comparison. For the Kirigami sheets, we found that friction initially increased with strain, which made for increasing friction with decreasing contact area. As the strain continued to increase the friction-strain curve exhibited highly non-linear trends with strong negative slopes as well (see Fig. 2.12). During the full strain, the contact area was decreasing monotonically except for a slight increase just before rupturing. These results contradict the asperity theory hypothesis of decreasing friction with decreasing contact area, and we conclude that no clear relationship between friction and contact area can be made. The non-cut sheet did not show any significant dependency on the strain as both the friction and the contact area remained constant with strain. Thus our findings suggest that a changing contact area and the strain-induced friction effects might be associated through an underlying mechanism connected to the buckling of the sheet. We did find some independent effects from the introduction of Kirigami cuts before applying strain. We observed a small increase in friction between the non-cut sheet and the Kirigami sheet, but this was one order of magnitude lower than the effects associated with the strain in combination. Since the strained non-cut sheet did not exhibit any significant effects from strain we conclude that the independent effects from Kirigami cuts and tension in the sheet cannot be regarded as a dominating mechanism for friction. When considering the friction dependency with load, we generally found a weak dependency corresponding to a friction coefficient on the order of 10^{-4} – 10^{-5} even though we could not confirm any clear relationship. This is best attributed to a superlubric state of the graphene sheet as seen in other studies as well. The slope of the friction-load curve was not considerably affected by the straining of the Kirigami sheet which led us to the conclusion that strain-induced effects are dominant in comparison to any load-related effects. In summary, we have found clear evidence that the friction in the Kirigami sheet system is controlled by strain.

When considering our findings in light of previous related results we find it plausible that the governing mechanism for the observed friction effects is related to commensurability. Since we have observed extremely low friction in our system, we argue that the non-deformed sheet corresponds to an incommensurable configuration. This is supported by the fact that we were not able to lower the friction from the original starting point. Additionally, this also aligns with the observation that the introduction of the non-strained Kirigami designs increased friction slightly. Since some atoms were removed from the lattice this can be hypothesized to relax the incommensurability to some degree. When the Kirigami sheet buckles during stretching, it allows for a considerable rearrangement of the atoms in contact with the substrate. Hence, it may transition in and out of commensurable configurations, which could explain the non-linear trend for the friction-strain curve. One way to test this hypothesis is to reorientate the sheet in order to reach a commensurable start configuration. Then we might find a transition from a commensurable to an incommensurable case during the initial straining which would result in a lowering in friction with respect to the starting point.

3.1.4 Capturing trends in friction data with machine learning

By utilizing the numerical framework for generating Kirigami design we have created a MD-based dataset for the frictional behavior depending on Kirigami designs, load and strain. The dataset reveals some general correlations with mean friction, such as a positive correlation to strain (0.77) and porosity (0.60), and a negative correlation to contact area (-0.67). These results align with the finding in the pilot study, suggesting that the change in friction is associated with cuts in the sheet (porosity) and a changing contact area.

By defining the friction property metrics: $\min F_{\text{fric}}$, $\max F_{\text{fric}}$, $\max \Delta F_{\text{fric}}$ and max drop (maximum decrease in friction with strain), we investigated the top design candidates within our dataset. From these results, we found no indication for the possibility to reduce friction with the Kirigami approach since the non-cut sheet provided the lowest overall friction. Furthermore, among the top candidates, we found that a flat friction-strain profile is mainly associated with little decrease in the contact area and vice versa. These observations are consistent with the results of the pilot study and support the hypothesis that commensurability plays a key role in governing the behavior of the system. In terms of the maximum properties, we observed an improvement compared to the values obtained in the pilot study, with the Honeycomb pattern exhibiting the highest scores. This indicates that the data may be useful for optimizing these properties.

For the machine learning investigation, we have implemented a VGGNet-16-inspired convolutional neural network with a deep “stairlike” architecture: C32-C64-C128-C256-C512-C1024-D1024-D512-D256-D128-D64-D32, for convolutional layers C with the number denoting channels and fully connected (dense) layers D with the number denoting nodes. The final model contains 1.3×10^7 parameters and was trained using the ADAM optimizer for a cyclic learning rate and momentum scheme. We trained the network for a total 1000 epochs while saving the best model during training based on the validation score. The model validation performance gives a mean friction R^2 score of $\sim 98\%$ and a rupture accuracy of $\sim 96\%$. However, we got lower scores for a selected subset of the Tetrahedon ($R^2 \sim 88.7\%$) and Honeycomb ($R^2 \sim 96.6$) pattern based on the top 10 max drop scores respectively. The scores obtained were lower, even though the selected configurations were partly included in the training data and the hyperparameter selection favored the performance on this selected set. Thus we conclude that these selected configurations, associated with a highly non-linear friction-strain curve, represent a bigger challenge for the machine learning prediction. One interpretation is that these involve the most complex dynamics and perhaps that this is not readily distinguished from the behavior of the other configurations which constitute the majority of the data set. By evaluating the ability of the model to rank the dataset based on property scores, we found that it was able to effectively represent the top three scores for the maximum categories. However, the ranking for the minimum friction property was lacking. We attribute this discrepancy to the fact that this property requires a higher level of precision, which the model was not able to achieve. To obtain a more accurate evaluation of the model’s performance, we generated a test set using MD simulations for the random walk based suggestions obtained from the accelerated search. The results showed a significantly worse performance compared to the validation set, with a two-order of magnitude higher loss and a negative R^2 score for the mean friction property. The negative R^2 score suggests that the model’s predictions were worse than simply predicting the mean value of the true data.

However, by reevaluating the hypertuning and choosing solely on the basis of validation loss, we still found poor results on the test set. This suggests that the inadequate performance is not solely due to biased hypertuning but rather because our original dataset did not sufficiently cover a diverse range of Kirigami configurations to accurately capture the full complexity of its frictional behavior. The validation scores indicate that the use of

machine learning is a feasible approach for addressing this problem, as we were able to identify some general trends in the data. Nonetheless, from the test scores, it is evident that further improvements to the dataset are necessary in order to develop a reliable model.

3.1.5 Accelerated search

Using the ML model we performed two types of accelerated search. One by evaluating the property scores of an extended dataset and another with the use of the genetic algorithm approach. For the extended dataset search, we used the developed pattern generators to generate 1.35×10^6 Tetrahedron, 2.025×10^7 Honeycomb and 10k Random walk patterns. The search results for the minimum friction property indicate a preference for low cut density or low porosity. This aligns with the overall observation that the dataset does not provide any suggestions to further reduction in friction, as the non-cut sheet has the lowest friction.

The search for the maximum properties resulted in some minor score increases but the suggested candidates were mainly overlapping with the original dataset. By investigating the sensitivity to translations of the Tetrahedron and Honeycomb patterns, we observed significant variations in the model's predictions with only minor translations. This can be attributed to a physical dependency since these translations affect the edge of the sheet. However, given the poor model performance on the test set, we believe it is more likely that this variation is due to an insufficiency in the model caused by the limitations of the dataset.

In our investigation of the genetic algorithm approach, we used a starting population that was based on the results from the extended dataset accelerated search, as well as some randomly generated initializations with different porosity values. However, this approach did not provide any noteworthy indication for new design structures worth more investigation. In general, the initialization of the population itself proved to be a more promising strategy than the genetic algorithm. We acknowledge that further effort could potentially yield useful results with the genetic algorithm approach. However, we believe that the current lack of promising results can be attributed to the uncertainty of the model which where the reason for not pursuing this any further.

By considering the Grad-CAM explanation method, we observed that the model predictions were often substantially reliant on the top and bottom edges of the Kirigami configurations. This was unexpected since these edges are not true edges but are connected to the pull blocks used in the simulation. Despite the model's uncertain predictions, we speculate that this may be due to the thermostat effects from the pull blocks. Therefore, we note this as a feature worth investigating in the simulations.

3.1.6 Negative friction coefficient

Based on our initial investigations of the Kirigami sheet, we have discovered a highly non-linear friction-strain relationship. By proposing a linear coupling between load and strain with ratio R , we find that these results suggest the possibility to utilize the negative slope on the friction-strain curve to achieve a negative friction coefficient. Based on the drop from top to bottom of these curves, using the Tetrahedron (7, 5, 1) and Honeycomb (2, 2, 1, 5) pattern from the pilot study, we estimate that the average coefficient within this range will be $-R12.75$ nN for the Tetrahedron pattern and $-R \cdot 2.72$ nN for the Honeycomb pattern.

To investigate this hypothesis, we conducted a simulation with a coupling between load and sheet tension, mimicking a nanomachine attached to the sheet, using the Kirigami configurations from the Pilot study. We observed that the non-linear behavior in the friction-strain curve also translated into a non-linear friction-load relationship for the coupled system. Additionally, we found that the Honeycomb pattern exhibited a non-linear strain-tension curve which resulted in an almost discontinuous increase in friction for the initial increase in load. We attribute this feature to an unfolding process visually confirmed from the simulation frames. For the coupled system with a load-to-tension ratio of 6 we found regions in the friction-load curve with significant negative slopes. By considering the maximum and minimum points for such regions we estimated the average friction coefficient to be -0.31 in the load range $F_N = [4.65, 6.55]$ nN for the Tetrahedron pattern and -0.38 in the range $F_N = [0.71, 4.31]$ nN for the Honeycomb pattern. These results can be scaled by adjusting the load-to-tension ratio.

Based on our investigations, we have found that the combination of Kirigami cuts and strain has significant potential for controlling friction. Specifically, we have demonstrated that by enforcing a coupling between load and strain through tension, it is possible to achieve a negative friction coefficient. Therefore, we believe that this approach could be promising for developing novel friction-control strategies.

3.2 Outlook

In this thesis, we have demonstrated that certain Kirigami designs exhibit non-linear friction behavior with strain. This discovery was made through an exploration of different designs, which invites further investigation into the underlying mechanisms of this phenomenon. To this end, it would be valuable to one or two selected designs, such as the Tetrahedron and Honeycomb patterns, and study the effects of various physical parameters on the friction-strain curve.

First of all, we suggest an investigation of how the friction-strain curve depends on temperature, sliding speed, spring constant, and loads for an increased range $F_N > 100nN$. This is especially interesting in the context of physical conditions leading to a stick-slip behavior since our study takes a basis in smooth sliding friction. Moreover, it would be valuable to verify that the choices for relaxation time, pauses, interatomic potentials and substrate material are not critical for the qualitative observations. Especially the Adaptive Intermolecular Reactive Empirical Bond Order (AIREBO) potential for the modeling of the graphene sheet might be of interest. In this context, it might also be useful to investigate the effects of excluding adhesion from the simulations.

In order to investigate the hypothesis of commensurability as a governing mechanism we suggest an investigation of the friction-strain curve for different scan angles. If commensurability is an important factor, we hypothesize that the friction-strain curve will exhibit different qualitative shapes at varying scan angles. Additionally, it may be interesting to investigate the friction-strain relationship under a uniform load to gain insight into how the loading distribution affects the out-of-plane buckling and associated commensurability effect.

Another topic worth studying is the relation to scale and edge effects. This includes an investigation of scaling effects, considering the ratio of the sheet area to the edge length, but also a translation of the sheet patterns to study the presence of any Kirigami-induced edge effects. The latter is motivated by the findings from the machine learning predictions. With this regard, we would also suggest a more detailed study of the effect of the thermostat in the pull blocks which is suggested to have a possible importance when judging from the Grad-CAM analysis.

Regarding the machine learning approach, our findings indicate that there is a significant need to expand the dataset. In order to get more insight into this issue one could use unsupervised clustering techniques like the t-Distributed Stochastic Neighbor Embedding (t-SNE) to visualize the distribution of Kirigami configurations in the dataset. Another valuable approach is the active learning method similar to that used by Hanakata et al. [6]. That is, we extend the dataset using the top candidates of a machine learning-driven accelerated search and repeat the process of training the model, searching for new candidates and extending the dataset. This provides a direction for the extension of the dataset which could lead to a more efficient approach to address the complex space of Kirigami designs. We note that one can also create a dataset of a fixed kirigami designs and vary the physical parameters to support the investigations mentioned above. For both variations we believe that the results could benefit from a consideration of more advanced model architectures and machine learning techniques. If successful this would invite further studies of inverse design methods such as GAN or diffusion models.

Appendices

Appendix A

Appendix A

Appendix A

Appendix B

Appendix B

Appendix C

Bibliography

- ¹E. Gnecco and E. Meyer, *Elements of friction theory and nanotribology* (Cambridge University Press, 2015).
- ²Bhusnan, “Introduction”, in *Introduction to tribology* (John Wiley & Sons, Ltd, 2013) Chap. 1, 1–?
- ³H.-J. Kim and D.-E. Kim, “Nano-scale friction: a review”, *International Journal of Precision Engineering and Manufacturing* **10**, 141–151 (2009).
- ⁴K. Holmberg and A. Erdemir, “Influence of tribology on global energy consumption, costs and emissions”, *Friction* **5**, 263–284 (2017).
- ⁵B. Bhushan, “Gecko feet: natural hairy attachment systems for smart adhesion – mechanism, modeling and development of bio-inspired materials”, in *Nanotribology and nanomechanics: an introduction* (Springer Berlin Heidelberg, Berlin, Heidelberg, 2008), pp. 1073–1134.
- ⁶P. Z. Hanakata, E. D. Cubuk, D. K. Campbell, and H. S. Park, “Accelerated search and design of stretchable graphene kirigami using machine learning”, *Phys. Rev. Lett.* **121**, 255304 (2018).
- ⁷P. Z. Hanakata, E. D. Cubuk, D. K. Campbell, and H. S. Park, “Forward and inverse design of kirigami via supervised autoencoder”, *Phys. Rev. Res.* **2**, 042006 (2020).
- ⁸L.-K. Wan, Y.-X. Xue, J.-W. Jiang, and H. S. Park, “Machine learning accelerated search of the strongest graphene/h-bn interface with designed fracture properties”, *Journal of Applied Physics* **133**, 024302 (2023).
- ⁹Y. Mao, Q. He, and X. Zhao, “Designing complex architected materials with generative adversarial networks”, *Science Advances* **6**, eaaz4169 (2020).
- ¹⁰Z. Yang, C.-H. Yu, and M. J. Buehler, “Deep learning model to predict complex stress and strain fields in hierarchical composites”, *Science Advances* **7**, eabd7416 (2021).
- ¹¹A. E. Forte, P. Z. Hanakata, L. Jin, E. Zari, A. Zareei, M. C. Fernandes, L. Sumner, J. Alvarez, and K. Bertoldi, “Inverse design of inflatable soft membranes through machine learning”, *Advanced Functional Materials* **32**, 2111610 (2022).
- ¹²S. Chen, J. Chen, X. Zhang, Z.-Y. Li, and J. Li, “Kirigami/origami: unfolding the new regime of advanced 3D microfabrication/nanofabrication with “folding””, *Light: Science & Applications* **9**, 75 (2020).
- ¹³OpenAI, *Dall-e2*, 2023.
- ¹⁴Midjourney, *Midjourney*, 2023.
- ¹⁵Z. Deng, A. Smolyanitsky, Q. Li, X.-Q. Feng, and R. J. Cannara, “Adhesion-dependent negative friction coefficient on chemically modified graphite at the nanoscale”, *Nature Materials* **11**, 1032–1037 (2012).
- ¹⁶B. Liu, J. Wang, S. Zhao, C. Qu, Y. Liu, L. Ma, Z. Zhang, K. Liu, Q. Zheng, and M. Ma, “Negative friction coefficient in microscale graphite/mica layered heterojunctions”, *Science Advances* **6**, eaaz6787 (2020).
- ¹⁷D. Mandelli, W. Ouyang, O. Hod, and M. Urbakh, “Negative friction coefficients in superlubric graphite–hexagonal boron nitride heterojunctions”, *Phys. Rev. Lett.* **122**, 076102 (2019).
- ¹⁸R. W. Liefferink, B. Weber, C. Coulais, and D. Bonn, “Geometric control of sliding friction”, *Extreme Mechanics Letters* **49**, 101475 (2021).
- ¹⁹M. Metzsch, *Tuning Frictional Properties of Kirigami Altered Graphene Sheets using Molecular Dynamics and Machine Learning*.

- ²⁰A. P. Thompson, H. M. Aktulga, R. Berger, D. S. Bolintineanu, W. M. Brown, P. S. Crozier, P. J. in 't Veld, A. Kohlmeyer, S. G. Moore, T. D. Nguyen, R. Shan, M. J. Stevens, J. Tranchida, C. Trott, and S. J. Plimpton, “LAMMPS - a flexible simulation tool for particle-based materials modeling at the atomic, meso, and continuum scales”, *Comp. Phys. Comm.* **271**, 108171 (2022).
- ²¹E. M. Nordhagen, *LAMMPS simulator*.
- ²²A. H. Larsen, J. J. Mortensen, J. Blomqvist, I. E. Castelli, R. Christensen, M. Dułak, J. Friis, M. N. Groves, B. Hammer, C. Hargus, E. D. Hermes, P. C. Jennings, P. B. Jensen, J. Kermode, J. R. Kitchin, E. L. Kolsbjerg, J. Kubal, K. Kaasbjerg, S. Lysgaard, J. B. Maronsson, T. Maxson, T. Olsen, L. Pastewka, A. Peterson, C. Rostgaard, J. Schiøtz, O. Schütt, M. Strange, K. S. Thygesen, T. Vegge, L. Vilhelmsen, M. Walter, Z. Zeng, and K. W. Jacobsen, “The atomic simulation environment—a python library for working with atoms”, *Journal of Physics: Condensed Matter* **29**, 273002 (2017).
- ²³A. Paszke, S. Gross, F. Massa, A. Lerer, J. Bradbury, G. Chanan, T. Killeen, Z. Lin, N. Gimelshein, L. Antiga, A. Desmaison, A. Kopf, E. Yang, Z. DeVito, M. Raison, A. Tejani, S. Chilamkurthy, B. Steiner, L. Fang, J. Bai, and S. Chintala, “Pytorch: an imperative style, high-performance deep learning library”, in *Advances in neural information processing systems 32* (Curran Associates, Inc., 2019), pp. 8024–8035.
- ²⁴S. Li, Q. Li, R. W. Carpick, P. Gumbsch, X. Z. Liu, X. Ding, J. Sun, and J. Li, “The evolving quality of frictional contact with graphene”, *Nature* **539**, Number: 7630, 541–545 (2016).
- ²⁵H. M. Yoon, Y. Jung, S. C. Jun, S. Kondaraju, and J. S. Lee, “Molecular dynamics simulations of nanoscale and sub-nanoscale friction behavior between graphene and a silicon tip: analysis of tip apex motion.”, *Nanoscale* **7** 14, 6295–303 (2015).
- ²⁶Y. Liu, F. Grey, and Q. Zheng, “The high-speed sliding friction of graphene and novel routes to persistent superlubricity”, *Scientific Reports* **4**, 4875 (2014).
- ²⁷P. Zhu and R. Li, “Study of nanoscale friction behaviors of graphene on gold substrates using molecular dynamics”, *Nanoscale Research Letters* **13**, 34 (2018).
- ²⁸J. Zhang, E. Osloub, F. Siddiqui, W. Zhang, T. Ragab, and C. Basaran, “Anisotropy of graphene nanoflake diamond interface frictional properties”, *Materials* **12**, 10.3390/ma12091425 (2019).
- ²⁹F. Bonelli, N. Manini, E. Cadelano, and L. Colombo, “Atomistic simulations of the sliding friction of graphene flakes”, *The European Physical Journal B* **70**, 449–459 (2009).
- ³⁰S. Zhang, Y. Hou, S. Li, L. Liu, Z. Zhang, X.-Q. Feng, and Q. Li, “Tuning friction to a superlubric state via in-plane straining”, *Proceedings of the National Academy of Sciences* **116**, Publisher: Proceedings of the National Academy of Sciences, 24452–24456 (2019).
- ³¹J. H. Dieterich, “Time-dependent friction in rocks”, *Journal of Geophysical Research (1896-1977)* **77**, 3690–3697 (1972).
- ³²R. Guerra, U. Tartaglino, A. Vanossi, and E. Tosatti, “Ballistic nanofriction”, *Nature Materials* **9**, 634–637 (2010).
- ³³H. Tomaç, Z. Guchan, and N. Altun, “How the stiletto heeled shoes which are popularly preferred by many women affect balance and functional skills?”, *Health Care for Women International* **43**, 1–11 (2020).
- ³⁴K. Gibbs, *Pressure*, (2020) https://www.schoolphysics.co.uk/age16-19/Mechanics/Statics/text/Pressure_/index.html.
- ³⁵F. B. Ltd, *Foot facts*, (2023) <https://www.footbionics.com/Patients/Foot+Facts.html>.
- ³⁶H.-J. Kim and D.-E. Kim, “Molecular dynamics simulation of atomic-scale frictional behavior of corrugated nano-structured surfaces”, *Nanoscale* **4**, 3937–3944 (2012).
- ³⁷M. Dienwiebel, N. Pradeep, G. S. Verhoeven, H. W. Zandbergen, and J. W. Frenken, “Model experiments of superlubricity of graphite”, *Surface Science* **576**, 197–211 (2005).